Order Number 9405589

Spectroscopic studies of the microstructure and distribution of photodeposited metal oxides in porous vycor glass

Sunil, Dehipawalage, Ph.D.

City University of New York, 1993

U·M·I
300 N. Zeeb Rd.
Ann Arbor, MI 48106

SPECTROSCOPIC STUDIES OF THE MICROSTRUCTURE AND DISTRIBUTION OF PHOTODEPOSITED METAL OXIDES IN POROUS VYCOR GLASS

by

Dehipawalage Sunil

A dissertation submitted to the Graduate Faculty in Physics in partial fulfillment of the requirements for the degree of Doctor of Philosophy, The City University of New York.

1993

This manuscript has been read and accepted for the Graduate Faculty in Physics in satisfaction of the dissertation requirement for the degree of Doctor of Philosophy

9/23/93

Date

M. H. Rafailovich

Chair of Examining Committee

Prof. M.H.Rafailovich

9/28/93

Date

Joseph B. Krieger

Executive Officer

Prof.J.Krieger

Prof. M.L.denBoer

Prof.H.D.Gafney

Prof.R.Gambino

Prof.N.Garcia

Supervisory committee

The City University of New York

Abstract

SPECTROSCOPIC STUDIES OF THE STRUCTURE AND DISTRIBUTION OF PHOTODEPOSITED METAL OXIDES IN POROUS VYCOR GLASS

by

Dehipawalage Sunil

Advisor:Professor Miriam. H. Rafailovich

The microscopic structure, distribution, bond length, co-ordination of photodeposited Fe in Porous Vycor Glass(PVG) has been studied by several spectroscopic techniques:Extended X-ray Absorption Fine Structure(EXAFS) spectroscopy, Mossbauer spectroscopy, Rutherford Backscattering spectroscopy(RBS), X-ray microprobe and Transmission Electron Microscopy(TEM). Although the photolysis and subsequent heatings are carried out in air, spectroscopic data reveal two surprisingly different forms of iron. One is similar to α-Fe_2O_3 and consists of an Fe^{3+} ion octahedrally surrounded by six oxygen atoms at a distance of 1.8 Å. The second compound which comprises more than 50% of the reaction product, is mainly elemental Fe, in which a central Fe atom is surrounded by another set of iron atoms at a distance of 2 Å. Heating to 650^{0}C or 1200^{0}C has

only little effect on product type, ratio, or distribution. But the size of the Fe particles increases with temperature. After heating to 1200°C, particles are large enough to show magnetic hyperfine fields at room temperature. The observed hyperfine fields are 370 and 425 kG. The deviations of these values from the bulk values can be explained from the effect of particle size and interaction of surface atoms with the surrounding matrix.

Dedication

This dissertation is dedicated to my parents who work so hard to educate us.

Acknowledgements:

I would like to take this opportunity express my sincere thanks to my advisors Profs Miriam Rafailovich and Jon Sokolov for their encouragement, guidance and constant support which served me well last several years. They were always supportive, giving and ready to help not only for the research work but also any other occasion that I need help. I would also like to thank Dr N.F.Borelli of Corning glass of and valuable discussions. I am very happy to thank Prof. Marten den Boer of Hunter College of C.U.N.Y for serving in my committee and great help given to me for EXAFS analysis. He provides his data analysis program and helps me to collect data. He was always ready to spend his valuable time to discuss results and help me to solve difficult problems. I would also like to thank prof. Harry Gafney of chemistry department of Queens College for his close guidance, suggestions, and valuable discussions through out this project. I am indebted Prof. Narcio Garcia, our foreign student advisor, for serving in my committee, his guidance, valuable advises and kind help given to me from the beginning of my graduate studies at Queen College. He always look after our support and ready help us any time and do what ever he can to solve our problems. I would like to express my sincere thanks to Prof. R. Gambino for serving in my committee with a very short notice and for the magnetization measurements. I am deeply thankful to Prof

Barry Wilkens of Bellcore for helping me to learn about and do RBS and Pixe experiments and helping us to run several samples. I would also like to express my sincere thanks to Dr.David Hwang of Bellcore for teaching me basics of TEM and helping me to take pictures despite of his limited time availability. He was always ready to help when I need it. I would also like thank prof.K.Rafanelli and Physics department for supporting me for the entire period of my graduate studies. I also like to thank Ms X.Duan and Ms S.Fan of Chemistry department for preparation of samples of PVG for these various experiments. I would also like to thank Mr Leonad Cannone of Geology department for grinding the glass samples. He was very helpful and and always ready to help despite of his various other jobs. Without their help it is impossible to complete this work. I would also like to thank Mr.Paul Schaedler and Mr.Ed Kuhner for the machine shop works. I would also like to thank my long time friends Mr Ananda Pannila who first encourage me for graduate studies and Dr Mahendra Kahanda and Dr Ananda Amarasinghe for helping me to come to the U.S.A. I would also like thank all of my graduate, undergraduate, and school teachers for their teachings, advises and showing me the right direction. Specially I like to thank Mr. H. Abeyrathne, my high school Physics and Maths teacher. If I didn't meet him it is even not possible me to pass the university entrance examination. It is impossible to

mention all the supporters by names therefore I would like to thanks all again mentioned and unmentioned supporters and friends for their help. Last, but not least I would like to thank my parents, my brothers and sisters, my dearest daughter Sumudu, my lovely son Shaliya who miss me so much, some times even seen me several days, and my wife Nandanee for providing me moral support during very long entire period of my graduate studies.

Table of contents

List of Tables

List of figures.

INTRODUCTION

The deposition of high resolution patterns of metals and metal oxides on glass and glass gels which are capable of creating refractive index gradients for the use of integrated optics and optical devices has been a topic of extensive study in the past several years[1-5]. One approach to produce these patterns is photolysis of organometallic precursors absorbed onto porous glasses followed by thermal consolidation to a non porous glass. Photodeposition yields patterns of high resolution(< 1μm) in Porous Vycor Glass(PVG) and base catalyzed tetramethoxysilane/ methanol/ water (TMOS/MeOH/H_2O) xerogels[4]. Consolidation reduces the sample volume by as much as 40%, but surprisingly, it occurs with no detectable loss in pattern resolution. In both glasses, photolysis creates a nonvolatile adsorbate within the pores of the glass which is then entrapped in the consolidating matrix. Deposition changes the density of the glass and, in turn, its refractive index. As a result, relatively straightforward photolithographic techniques yield structures capable of guiding, focusing and diffracting light[3,4]. In order to develop devices incorporating these structures, however, it is important to understand the chemical and physical properties and microstructure of the photo products and their distribution within the glass matrix. It should be emphasized though at

this point that the photolysis method of producing metallic glasses is fundermentally different from the techniques used to produce Fe-silicate glasses previously studied[6-12]. Those glasses were formed by mixing iron oxides together with the glass former prior to annealing. The resulting iron concentration and precipitation were then a function of the solubility of Fe in glass. In addition, the chemical configuration and the location of the Fe ions were in some cases a function of the particular glass formers used. In the photolysis method, the Fe ions are introduced after the glass is fully formed. The binding sites of the Fe ions are controlled by surface functionalities of the glass. The Fe ions are concentrated in the glass pores, and thus even though the total Fe concentration in the glass may be low (less than a few percent), the local concentration in the pores is high. The particle size can then be controlled either by varying the loading concentration or the pore size morphology. Since Fe compounds are formed primarily by the photolysis process, the chemical composition will depend mostly on the nature of the adsorbates on the glass surface, rather than the specific annealing temperature and environment used to form the glass.

In order to understand the chemical processes and identify the Fe compounds formed by photolysis, and subsequent consolidation of the glass, PVG impregnated with $Fe(CO)_5$ was studied by a variety of complementary analytical

techniques. Since the introduction of the $Fe(CO)_5$ is done by vapor deposition and hence is non-stoichiometric, the Fe concentration relative to silicon was first determined by Rutherford Backscattering Spectrometry(RBS). The distribution of Fe ions in the glass before and after photolysis and after heating processes was measured by x-ray microprobe fluorescence. The co-ordination number, magnetic properties, chemical nature, and volume fraction of different Fe compounds formed by the photolysis procedure was measured by Mossbauer spectroscopy. The nature of nearest neighbor atoms, co-ordination numbers, and bond lengths were determined by Extended X-ray Absorption Fine Structure spectroscopy (EXAFS) studies. Pre-edge feature of X-ray Absorption Near Edge Structure (XANES) was used to further confirm the type of iron compounds and co-ordination numbers. Finally Transmission Electron Microscopy (TEM) used to study size of the Fe clusters formed in the glass as a function of the annealing temperature.

CHAPTER 1.

Rutherford back-scattering spectroscopy:

1.1. Introduction:

Rutherford back-scattering spectrometry(RBS) was used to determine the Fe concentration of the samples relative to Si. In RBS a beam of energetic ions is directed to the sample. The ions scattered back were collected and their energy was measured. The energy of back-scattered particles depends on the mass of the target atom and sample thickness. Therefore from the intensity and energy of the scattered particles the composition of the sample, distribution of components within the sample, and sample thickness(where scattering occurs) can be studied.

1.2. Basic theory:

Back-scattering is a two body elastic collision process. The energy transferred from a projectile(a mono-energetic ion beam from an accelerator) to a target atom can be calculated from conservation of energy and momentum laws. Consider a two body collision as shown in Figure 1.2.1 in which a particle with energy, mass, and velocity E_0, m_1, and V_0 respectively collide with an atom of mass m_2.

From the conservation of momentum,

$$m_1V_0 = m_1V_1 \cos\theta + m_2V_2 \cos\Phi \quad \text{-----(1a)}$$

$$m_1V_1 \sin\theta = m_2V_2 \sin\Phi \quad \text{-----(1b)}$$

From the conservation of energy,

$$\tfrac{1}{2}m_1V_0^2 = \tfrac{1}{2}m_1V_1^2 + \tfrac{1}{2}m_2V_2^2 \quad \text{-----(2)}$$

From the above equations we can calculate the energy of the back-scattered ions, E, as follows,

$E = K\,E_0$ ----(3)

where

$$K = \left[\frac{[m_1\cos\theta + (m_2^2 - m_1^2\sin^2\theta)^{1/2}]}{m_1 + m_2}\right]^2$$

The factor, K, depends on the masses m_1 and m_2, and the scattering angle θ. If we use a projectile of known mass m_1, and known energy E_0, by measuring the energy of scattered particles at angle θ we can determine the unknown mass m_2. Now consider a beam strikes a sample containing two kinds of atoms of masses A and B as shown in Figure 1.2.2[13]. Then the

particles, back-scattered from the surface of the target, have energies either E_A or E_B depending on the type of target atom from which they scatter. E_A and E_B can be written as $E_A=K_AE_0$ and $E_B=K_BE_0$. The signals appear on the energy scale in Figure 1.2.2 at positions E_A and E_B can be identified as coming from masses A and B, respectively, and the energy scale is then converted into a mass scale.

Only a small fraction of the beam will be scattered by surface atoms. Further scattering occurs from atoms located at successively deeper positions below the surface. In each case the collision can be treated as a binary collision and the energy immediately after such a collision is related to the energy immediately before the collision via the factor K. As particles move through the sample to reach the depth from which they elastically scatter, they loose energy inelastically. When the scattered particles emerge through the sample they continue to loose the energy. As shown in Figure 1.2.2, scattering from the A atoms which are below the surface will give signals at energies less than K_AE_0. From the scattering intensity of each type of atom we can determine the ratio of the number of atoms in the sample.

1.3. Results and discussion:

Typical RBS spectra of PVG samples unheated, heated to 650^{0}C, heated to 1200^{0}C are shown in Figures 1.3.1,1.3.2, 1.3.3 respectively. Using equation 3 we can calculate the α particles backscattered from Fe, Si, and O have energies $K_{Fe}E_0$, $K_{Si}E_0$, and K_OE_0 respectively. Their edges are shown in Figure 1.3.3. The dash line corresponds to a fit assuming the α particle is scattered from SiO_2Fe_X. The values of X from different samples are listed in the table 1.1. It should be noted that the unheated and heated to 650^{0}C samples have an excess oxygen over the stoichiometric value expected for glass. This is a reflection of the H_2O still trapped in the glass while it is porous. As can be seen from the figure 1.2.5 heating to 1200^{0}C consolidates the glass, and the excess H_2O is removed and fit to the SiO_2 portion is now perfect. The amount of Fe relative to silicon, in three different samples together with the corresponding annealing temperature are listed in table 1.1. From the figures it can be seen that there is more Fe near the surface of the unheated sample. In the sample heated to 650^{0}C the distribution of Fe from the surface to the interior of the sample is almost uniform. But in the consolidated(heated to 1200^{0}C) sample, the amount of Fe near the surface is higher than that of the interior of the sample which indicates migration of some Fe atoms as sample consolidated at 1200^{0}C. Figure 1.3.4 shows the variation of

amount of Fe, with temperature, in typical high, medium, and low loading samples.

Table 1.1: The amount of Fe relative to Si.

Temperature -> initial loading ⇓	unheated	650^{0}C	1200^{0}C
Low	0.02	0.007	0.008
Medium	0.08	0.03	0.02
High	0.2	0.05	0.03

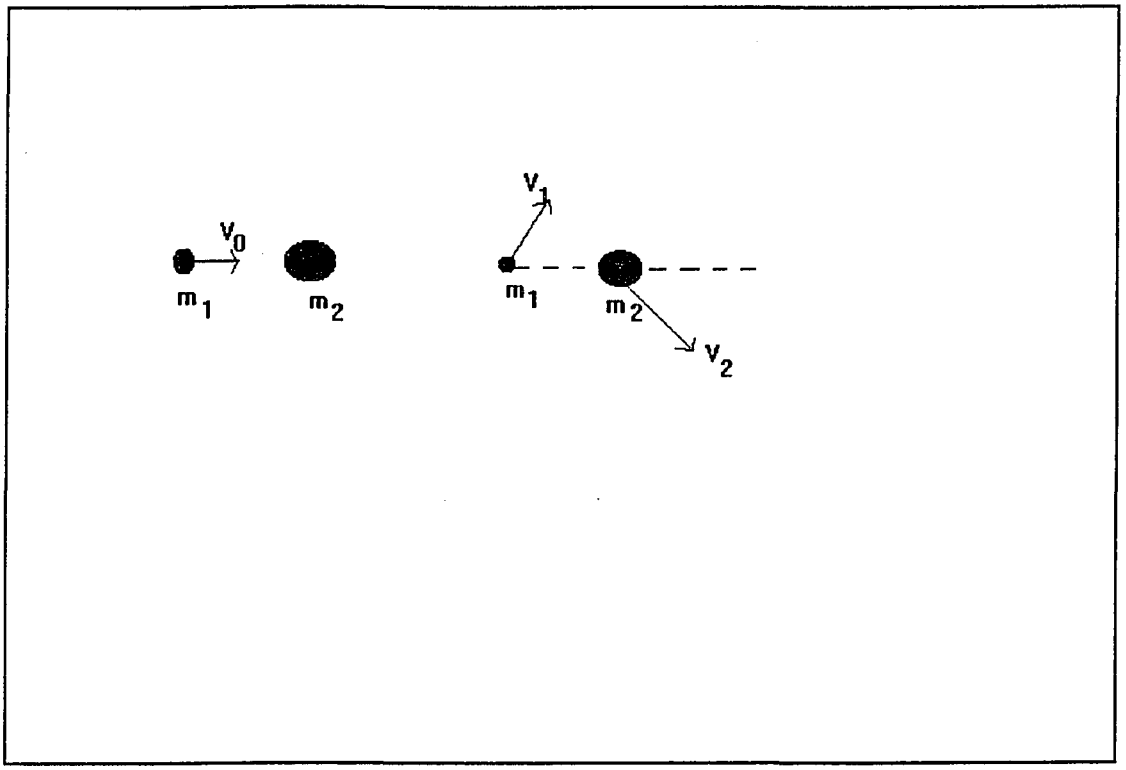

Figure 1.21. Scattering of an energetic particle after collision with an stationary atom.

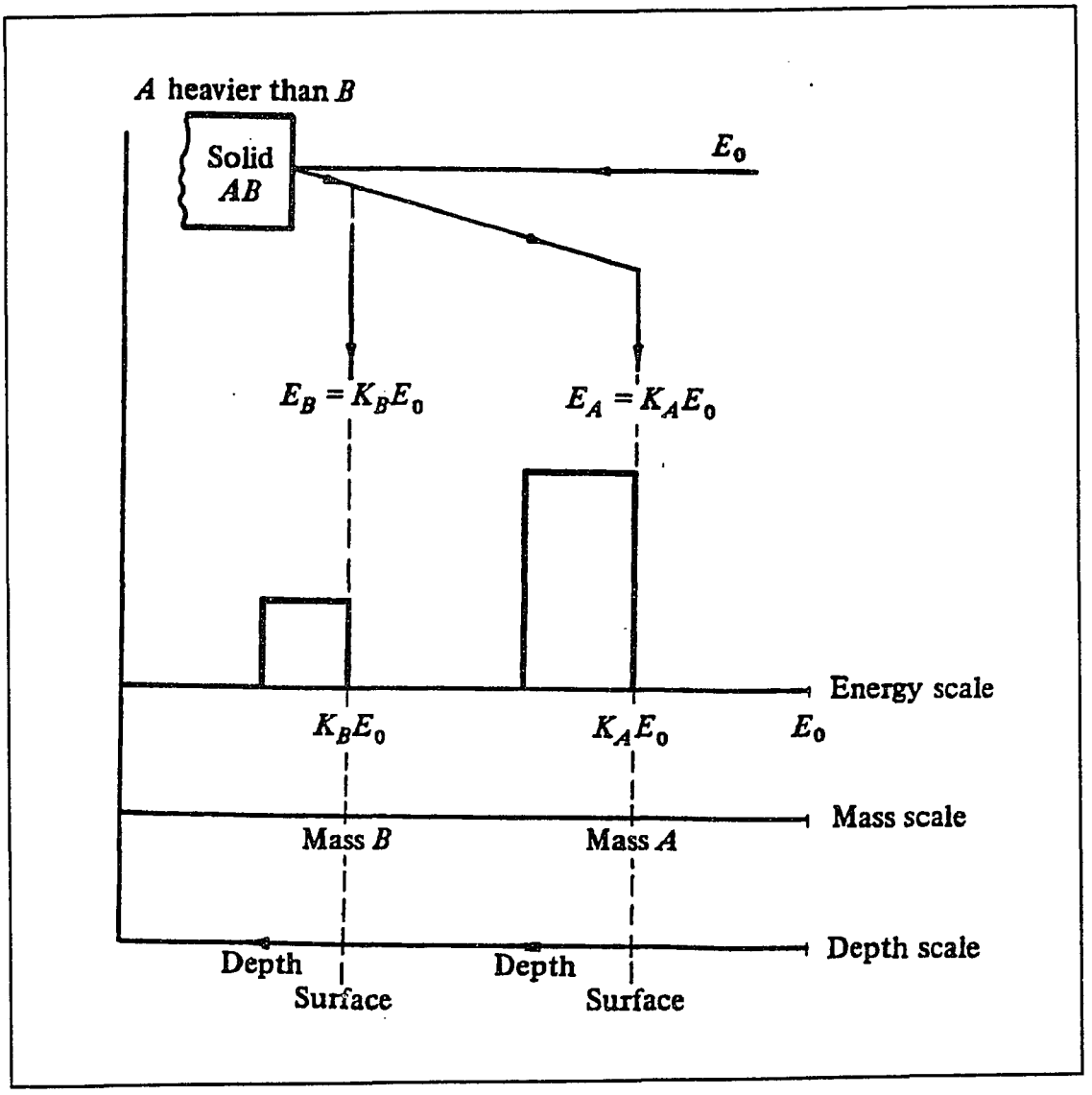

Figure 1.2.2. Rutherford backscattering from a solid composed of elements of mass A and B.

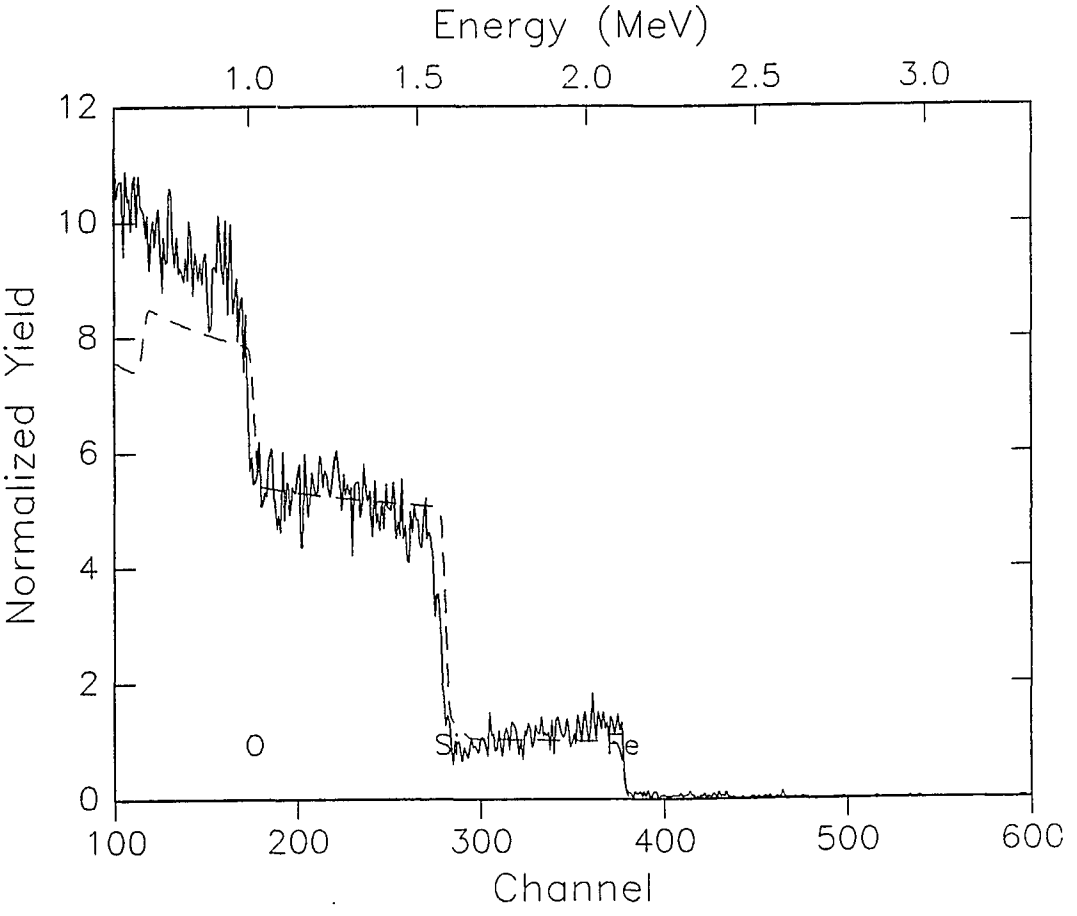

Figure 1.3.1 RBS spectrum of unheated PVG.

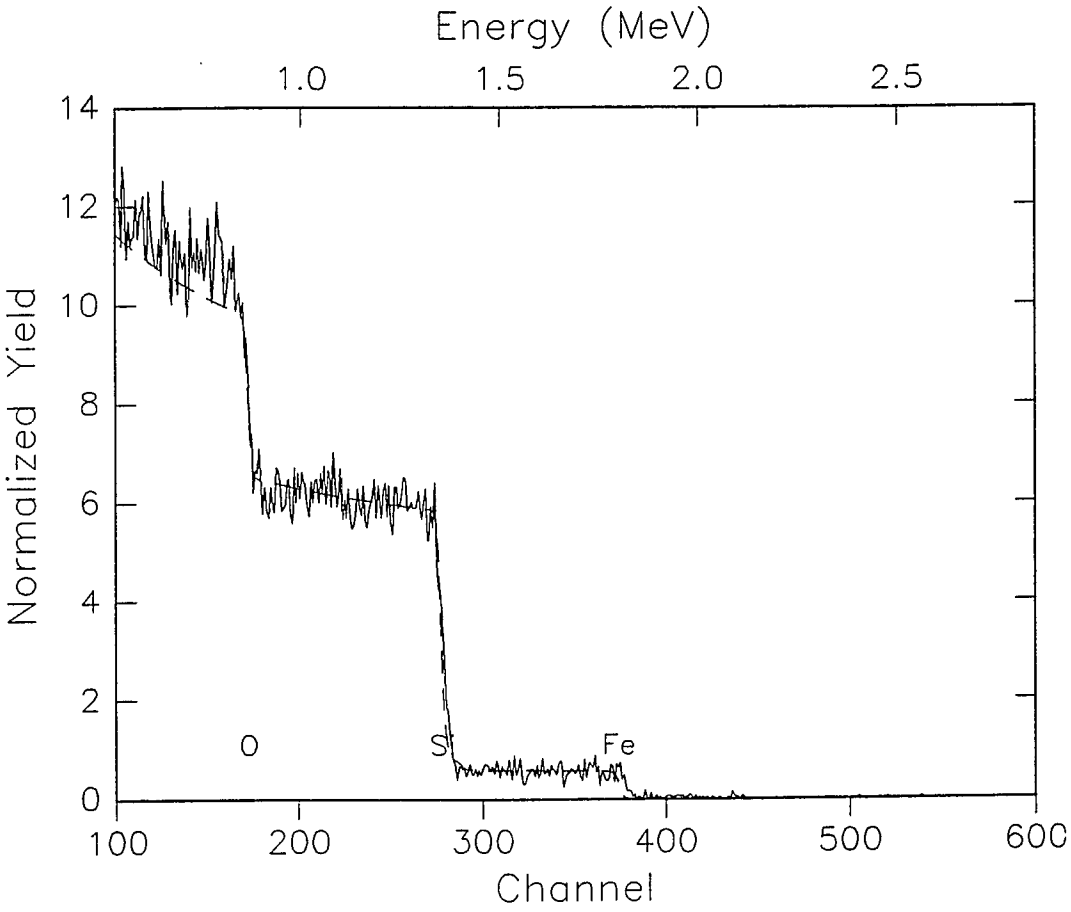

Figure 1.3.2 RBS spectrum of PVG heated to 650^{0}C.

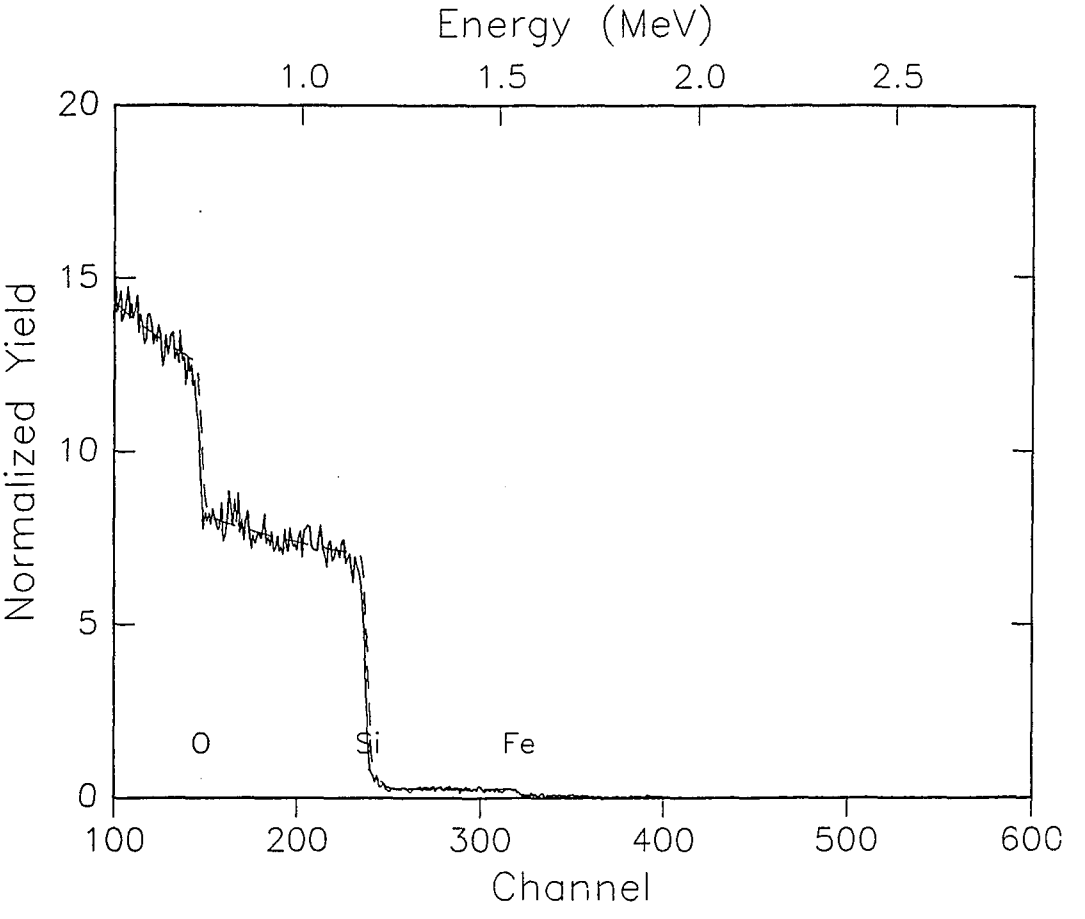

Figure 1.3.3 RBS spectrum of PVG heated to 1200.

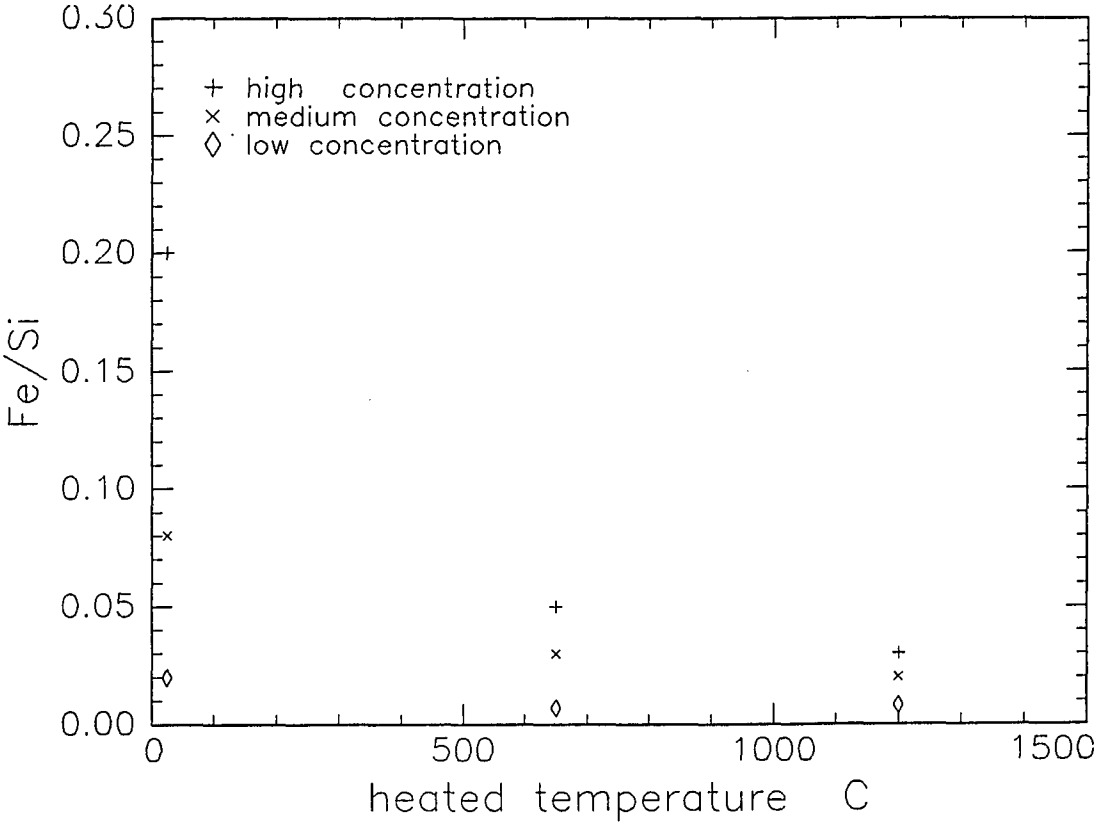

Figure 1.3.4. Variation of amount of Fe with temperature.

CHAPTER 2.

X-Ray fluorescence analysis.

The distribution of Fe in PVG was studied by X-ray microprobe fluorescence. An intense white X-ray beam of 20 microns in diameter, from beamline X-26 of Brookhaven National Laboratory National Synchrotron Light source(NSLS), was used to scan the edge of the PVG which was approximately 2 mm thick. The synchrotron radiation transfers its energy to the sample where different wave lengths are resonantly absorbed by different elements in the sample. The energy is then released when the system decays back to the ground state. Some of this energy is radiative,i.e., released as photons, thereby producing fluorescence. Since the fluorescence X-ray emission occurs when the decays involve core states, the photon energies correspond to values characteristics of the emitting element atomic core levels. Thus, x-ray fluorescence spectra can be used for qualitative and quantitative chemical analysis.

The distribution of Fe in PVG, before photolysis(Figure 2.1a), shows that $Fe(CO)_5$ penetrates uniformly at least to a depth of 2000 microns. Figure 2.1b shows the distribution of Fe in PVG after the photolysis. From the Figure 2.1b it can be seen that photolysis causes a significant change in the distribution of iron within the sample. After photolysis, the amount of Fe is largest near the surface.

The areas under curves a and b of Figure 2.1 are proportional to the amount of Fe in the sample. From the figures it can be seen that almost all the Fe in the unphotolysed sample remains in the sample after the photolysis. During photolysis the Fe atoms seem to migrate towards the surface of the sample. As the photolysis depletes the amount of $Fe(CO)_5$ near the surface, unreacted $Fe(CO)_5$ diffuses from the interior of the glass into the photodepleted regions, undergoes photodecomposition, and increases the amount of Fe near the surface. After the photolysis the general shape of the Fe distribution curves remains unchanged either after heating to 650^{0}C or heating to 1200^{0}C (Figure 2.2 and 2.3). From the Figures 2.2 and 2.3 it can be seen that the amount of Fe is relatively constant within the first 20 microns near the surface, which corresponds to the thickness of the samples used in EXAFS and Mossbauer experiments. The distribution of Fe in low concentration samples is fairly uniform upto 300 μm deep into the sample even after consolidation(Figure 2.3). The uniform region in low concentration sample is large enough to make mechanically stable samples. Photopattening in this region produces a well controlled gradient making commercial manufacture of these devices feasable.

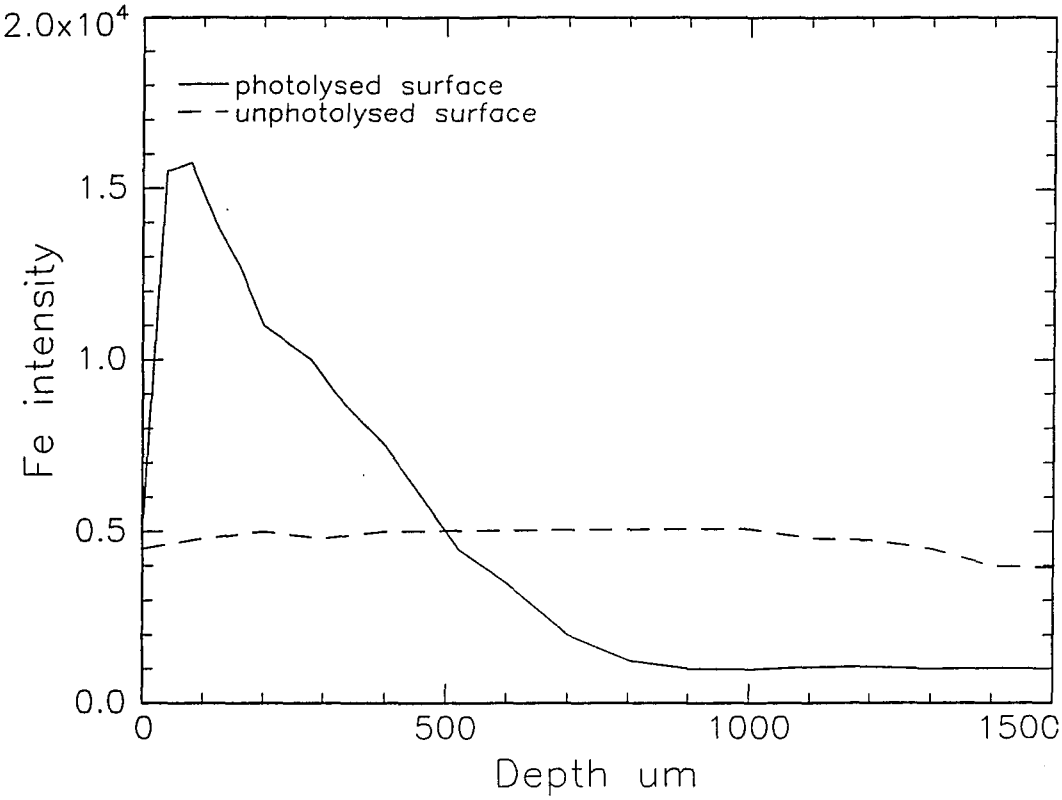

Figure 2.1. The distribution of Fe in PVG.
a) Photolysed surface
b) Unphotolysed surface.

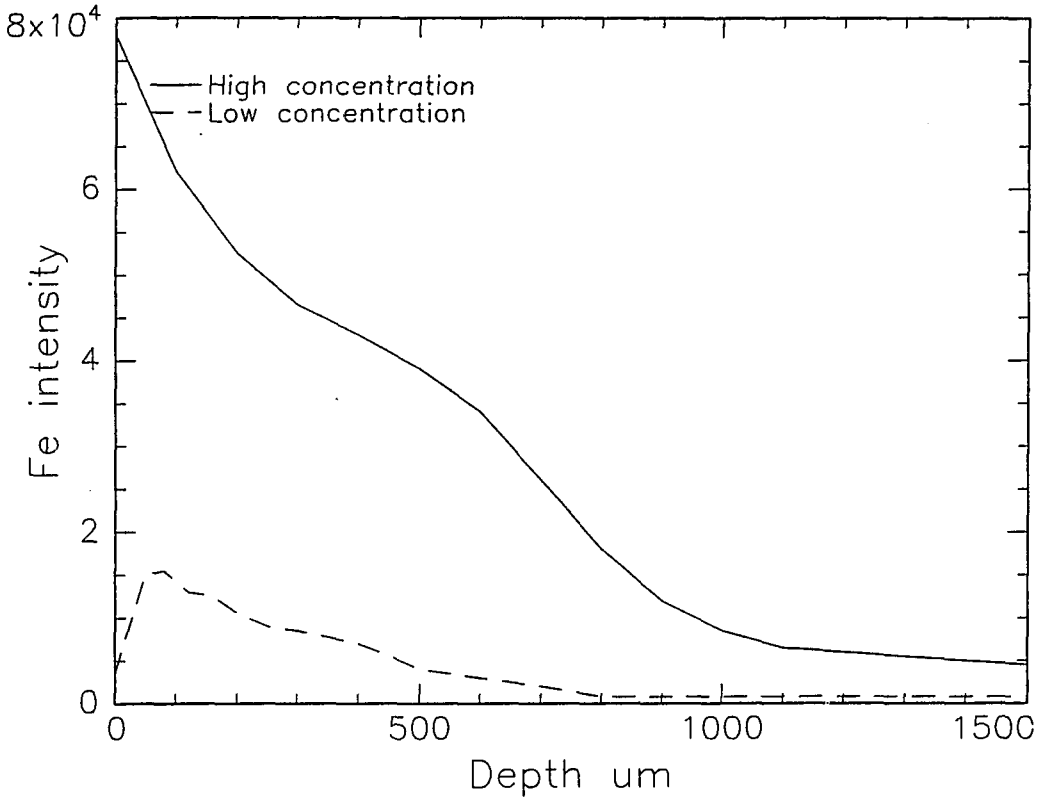

Figure 2.2. The distribution of Fe in PVG heated to 650°C.

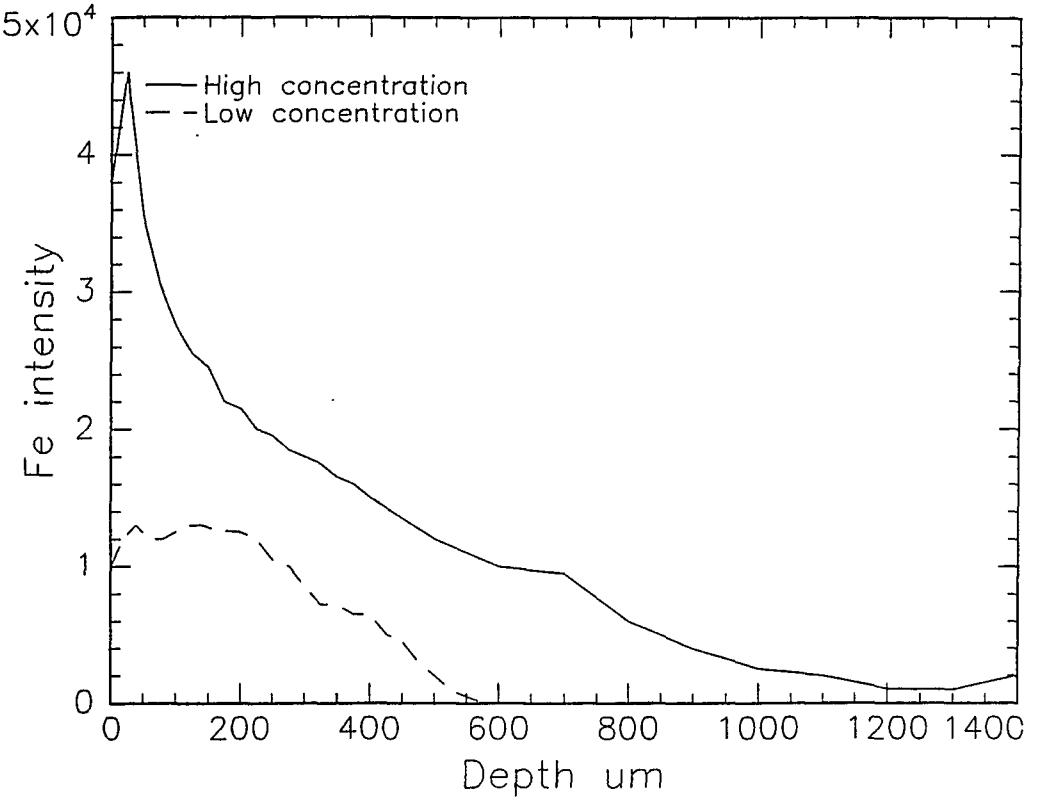

Figure 2.3. The distribution of Fe in PVG heated to 1200^{0}C.

CHAPTER 3.

Mossbauer spectroscopy.

3.1 An introduction to radioactivity

Radioactive isotopes which act as a source of radiation are essential to all Mossbauer experiments. Many elements in the periodic table have a number of isotopes which are radioactive. These isotopes decay to either stable, or other radioactive isotopes by emitting one or more particles or photons. The most common types of decays are termed beta(β), alpha(α) and gamma(γ) decay. In the case of Fe, the Mossbauer isotope, ^{57}Fe, is formed by electron capture from ^{57}Co. The reaction may be represented as

$$^{57}Co_{27} + {}^{0}\beta_{-1} \text{ ----------} {}^{57}Fe_{26} \text{ --------->} (1)$$

The ^{57}Fe formed in equation (1) is again in a nuclear excited state, and three gamma rays 14,123,137 keV are emitted on decay to the stable ^{57}Fe ground state (Figure 3.1.1). In addition to the gamma rays, x-rays are emitted as a consequence of the electron vacancy created after electron capture.

3.2 Nuclear Gamma Resonance;

The phenomena of Nuclear Gamma Resonance may occur between two nuclei, as shown in Figure 3.2.1, in their excited and ground states. The separation between two states represents the nuclear transition energy E_0. A nucleus of a source emits a γ-ray by transition from the excited state to the ground state. This γ-ray can be absorbed by another nucleus of the same kind by the reverse process.

Observation of Nuclear Gamma Resonance is difficult due to recoil of the nucleus. Consider a nucleus which is in an excited state energy, E_0, above the ground state energy. As it emits a gamma quantum to come to the ground state it experiences recoil with energy, E_R. Therefore the energy of the gamma quantum, E_γ, is given from the conservation of energy $E_\gamma=E_0-E_R$. Similarly as γ-ray absorbed by another atom looses part of its energy in transferring momentum of the absorber atom. E_R is always very small compared to the energy of the emitted photons but much greater than the natural line width of the γ-quantum. Therefore resonance absorption is hard to observe. Various methods have been used to improve the situation in γ-ray fluorescence by making the overlap between the emission and absorption curves larger and therefore increasing the yield of fluorescence, but none of them were successful.

It was Mossbauer's great discovery that for some low energy gamma rays E_R became negligible such that source and absorber energy profiles overlap completely[15]. In other words, emission of gamma rays occurs without recoil of the nucleus. In the simple Einstein model of a solid, the thermal properties of a lattice are described by the vibrational oscillations of the atoms with frequency, ν_E. The total energy of the system may be written as $E_t=h\nu_E(n+½)$ where n is the quantum number. If the recoil energy E_R is less than $h\nu$ the energy is not enough to excite the lattice and zero photon transition occurs. That means emission occurs without excitation of phonons in the lattice. Then the energy of the emitted gamma ray is almost equal to the transition energy since in this case the whole crystal mass recoils to conserve momentum. In practice this can be achieved as follows we take a suitable absorber-source pair such as Fe in stainless steel and ^{57} CO in stainless steel, vibrate the source over a range of velocities and count the number of gamma rays transmitted through the absorber at each velocity . At zero velocity the energy of emitted gamma rays is exactly equal to the energy difference between ground state and excited state and hence can be absorbed by the nuclei in absorber. But at velocities other than zero the energy of emitted gamma rays changes by $\Delta E=V_0/c\ E_\gamma$ due to the doppler effect. Therefore those gamma rays cannot be

absorbed by nuclei in the absorber. Therefore at zero velocity the count rate is a minimum and the spectrum looks like inset of Figure 3.2.1.

However, if one keeps the same single line source and changes the absorber, one or more peaks are observed, none of which in general will be at zero velocity due to hyperfine interactions. Introducing hyperfine interaction splits the energy levels in the absorber adding or subtracting ΔE to the ground state. This value is compensated by the Doppler shift and hence absorption occurs at velocities other than zero. As a result the absorption spectra can be used to determine the hyperfine interaction energies. The sources of these splittings are described in the next section.

3.3. Hyperfine parameters:

3.3.1. Isomer shift

The isomer shift or the chemical shift is the shift of the center of the Mossbauer spectrum from zero velocity. This results from the electrostatic interaction between the charge distribution of the nucleus and those electrons which have a finite probability of being found in the region of the nucleus. Only S electrons of the H-like orbitals have a finite probability of overlapping with the nuclear charge density. If the s electron density of the source and

absorber nuclei are different, the center of the Mossbauer spectrum shifts from the zero velocity. The s electron density of the resonating nuclei in the source and in the absorber can be varied by the chemical environment. By coulomb interaction the levels of the ground and of the excited state are changed, as indicated in the energy level diagram of Figure 3.3.1 ,and also the transition energies E_s and E_A.

E_0 can be considered as the hypothetical case of a point nucleus with the same charge. In the resonance experiment the difference between E_s and E_A is shown by the isomer shift. This shift can be expressed as[16,17]

$\delta = C\ \delta R/R\ [|\Psi_A(0)|^2 - |\Psi_s(0)|^2]$ where C is a constant for a given isotope, $\delta R/R$ is the relative change of the nuclear radius between excited state and ground state and $|\Psi_A(0)|^2$ and $|\Psi_s(0)|^2$ represents the electron density evaluated at the nucleus of the absorber and source respectively. Because the electron density at the nucleus is a function of the valence state and chemical bonding, Mossbauer isomer shift provides very useful method of examining the covalent character and determining the valency and oxidation state of the Mossbauer atom.

3.3.2. Quadrupole splitting

The interaction of the nuclear electric quadrupole moment eQ with the electric field gradient $V_{zz} = \partial^2 V/\partial Z^2$ at the site of the nucleus splits the nuclear state into sublevels with the eigen values[18]

$$E_Q = \frac{eQV_{zz}}{4I(2I-1)}[3m_I^2 - I(I+1)][1+\frac{\eta^2}{3}]^1/2$$

The asymmetry parameter η is given by $\eta = V_{xx} - V_{yy}/V_{zz}$. In the case of ^{57}Fe only the excited state, as shown in Figure 3.3.1 , splits with eigen values

$E_Q = \pm¼\ eQV_{zz}(1+\eta^2/3)^{½}$.

3.3.3. Nuclear Zeeman effect:

The interaction of the nuclear magnetic moment μ with a magnetic field H at the site of the nucleus splits the nuclear state with spin I into 2I+1 sublevels with eigen values $E_m = -\mu H m_I = -g_N \beta_N H m_I$ where m_I is the magnetic quantum number with the values $m_I = I, I-1, \ldots, -I$. The nuclear magnetic moment is related to the nuclear Bohr magneton β_N by the nuclear Lande g factor g_N by $\mu = g_N \beta_N I$.

In the case of ^{57}Fe, I=1/2 for the ground state and I=3/2 for the 14.4 keV first excited state. A magnetic field at the site of the nucleus causes a splitting of the nuclear states, as shown in energy level diagram in Figure 3.3.2.

The allowed transitions according to selection rules $\Delta m=0,\pm1$ leading to the six line pattern as shown in the Figure 3.3.2.

3.4. Data Analysis:

In order to obtain accurate values for parameters precise values of peak positions of the Mossbauer spectra are required. All the Mossbauer spectra are spread into 512 channels. From these, the first 51 channels corresponds to fly back of the velocity signal and therefore deleted from original data file. Then a parabolic function was fitted to the baseline and subtracted from the data to correct for the change in intensity due to source movement. Now curve fitting is used to find the peak positions, widths, intensities, and number of Lorentzian lines which when superimposed give the best fit to the observed envelope. The line shape y(x), of the envelope for a Lorentzian line is given by[19]

$$y(x)=b-\frac{y(0)}{1+(\frac{(x-x(0))}{\Gamma/2})^2}$$

where y(0) is the intensity at the resonance velocity x(0), Γ is the width at half height and b is the base line intensity. Thus the equation of the envelope for n lines becomes

$$y(x)=b-\sum_{i-1}^{n}\frac{y(0)_i}{1+(\frac{(x-x(0)_i)}{\Gamma/2})^2}$$

The data is then fit to the above equation and the parameters were varied until a minimum χ^2 is achieved.

3.5. Experimental setup:

A block diagram of the equipments is shown in Figure 3.5.1. The radioactive source was Co^{57} electroplated on to a Rh matrix. The energy spectrum emitted by this source is shown in Figure 3.5.2. From the energy spectrum only 14.4 keV line was selected using a suitable window in the single channel analyzer and used as multi channel scaling (MCS) input to the Nucleus personal computer analyzer (PCA) card. The source was attached to K-4 motor which is driven by asymmetric sawtooth wave generated by S-700A drive. The amplitude of the sawtooth wave determine the velocity scan of the vibrator. While the vibrator is sweeping continuously over the range of velocities, the multichannel analyzer is sweeping continuously through 512 channels with dwell time/channel 400μsec. The above two sweeps are automatically synchronized and gamma rays from a given velocity are always fed to the same channel in the analyzer.

3.6. Review of previous studies of Mossbauer spectroscopy of Fe in glasses:

The technique of ^{57}Fe Mossbauer spectroscopy has been widely used to characterize the structural role of iron in a broad range of glass compositions. The first indication of the usefulness of the Mossbauer effect to glasses were the studies done by Pollack et al[20], which demonstrated that glass is sufficiently rigid to enable resonant absorption of nuclear gamma rays to occur. The Mossbauer technique introduced the ability to determine iron site occupancies and gain insite into the structural characteristics of the materials being studied. Typical ranges of isomer shifts in glasses (relative to a metallic Fe standard) as a function of coordination number and valence state are given in table 3.1[21].

Table 3.1. Ranges of isomer shifts in glasses as a function of coordination number and oxidation state.

oxidation number	coordination number	isomer shift
Fe^{2+}	4	0.9-0.95 mm/s
	6	1.05-1.10 mm/s
	8	1.20-1.30 mm/s
Fe^{3+}	4	0.2-0.32 mm/s
	6	0.35-0.55 mm/s

Previous Mossbauer studies of Fe in glasses at room temperature show that in the case of low iron concentration (up to 30%) the Fe exists in a paramagnetic state independent of glass host and the method of preparation. Mossbauer experiments of Fe in silicate glasses show Fe to exist in Fe^{2+} or Fe^{3+} form with either tetrahedral or octahedral coordination. On the other hand, EXAFS data of Park and Chen[22] show only octahedral Fe^{3+} and no tetrahedral sites are observed. Eventhough room temperature Mossbauer patterns of these glasses are simple quadrupole doublets, they display hyperfine structure at low temperatures[23]. In general room temperature Mossbauer spectra of oxide glasses with more than 35% of Fe, shows magnetic hyperfine fields.

These hyperfine fields were assigned either to the simple iron oxides or ferrites. Some times these Mossbauer spectra are complicated and cannot account for any of the known iron compounds. As a example Bukrey and Kenealy[24] reported the hyperfine pattern of room temperature Mossbauer spectrum of a glass system with more than 35% of Fe_2O_3. The hyperfine field they observed was 265 KG. But the hyperfine structure of these high iron concentration glasses strongly is dependent upon sample preparation procedures and the glass system being studied. The quadrupole splitting of Mossbauer spectra is also useful to study the site symmetry of Fe ions. But unlike the isomer shift, quadrupole splitting alone cannot be used to identify the charge state or co-ordination number of Fe ions. In the case of Fe^{3+} ion($3d^5$) the electrons are spherically symmetrical and therefore will not contribute to the electric field gradient at the nucleus. Thus if the normal tetrahedral or octahedral co-ordination is undistorted no quadrupole splitting should be observed. But for Fe^{2+}ions quadrupole splitting is very large. This is due to axial or rhombic symmetry distortions generated by the d electron out side the half filled spherical shell. Quadrupole splitting is also dependent on the size of the particles. Kundig et al[25] have measured the Mossbauer spectra of fine α-Fe_2O_3 particles as a function of particle size, and have shown that the quadrupole splitting increases with decreasing particle size. It is generally

believed that on the surface of fine particles the ion sites have low symmetry and are therefore distorted considerably compared with bulk crystals. Yoshioka et al[26] have reported that the quadrupole splitting of surface atoms of fine α-Fe_2O_3 is about twice as large as that of bulk atoms. Levy[27] has reported that quadrupole splitting of the Fe^{3+} cations(in silicate glass) in tetrahedral co-ordination was roughly twice as large as that of the Fe^{3+} cations in octahedral co-ordination. The quadrupole splittings of Fe in glasses reported by several workers[28] is summarized in table 3.2.

Table 3.2. Quadrupole splitting values of Fe in glasses.

Ion	co-ordination number	Quadrupole splitting
Fe^{2+}	4	2-2.6 mm/s
	6	1.8-1.9 mm/s
Fe^{3+}	4	0.8-1.6 mm/s
	6	0.2-0.8 mm/s

3.7. Results and Discussion:

Mossbauer spectra of unphotolyzed and heated to 650^{0}C samples are completely featureless(Figure 3.7.1) and indicate that there is no Fe left in these samples. After photolysis spectra of PVG samples show quadrupole doublets (Figure 3.7.2 and 3.7.3) typical of Fe in Glass. The splittings are unaffected by either heating to 650^{0}C or cooling down to liquid nitrogen temperature. The dashed lines in the Figures show the Lorentzian doublets that produced the best fit to these spectra. Two separate Lorentzian doublets of unheated and heated to 650^{0}C samples indicate that the Fe exists at two different sites. But spectra of high concentration consolidated samples show hyperfine structure (Figure 3.7.4) instead of quadrupole splittings. Best fit of this spectrum was obtain using 12 Lorentzian lines. These lines, we can assume, are due to two separate Fe ions at two different sites or due to two separate iron compounds. Magnetic hyperfine fields obtained from these line positions are 370 and 425 KG. The isomer shifts and quadrupole splittings of these lines, designated as A and B, are listed in Table 3.3.

Table 3.3. Hyperfine parameters of Mossbauer spectra

Sample	Isomer shift		Q.S.		Line Width
	A	B	A	B	
Unheated	0.47	0.14	0.70	0.57	0.22
Heated to 650^{0}C	0.57	0.13	0.58	0.58	0.21
Heated to 1200^{0}C	0.41	0.16	0.11	0.11	0.20

All velocities are in mm/s.

Isomer shift is relative to metallic iron.

From both isomer shifts and quadrupole splitting values, listed in the Table 3.3, it is clear that A lines of both unheated and heated to 650^{0}C samples corresponds to octahedrally co-ordinated Fe^{3+} ions. Since the isomer shift of the A lines is smaller than that of B lines one is tempted to assume that the B lines are due to tetrahedrally co-ordinated Fe^{3+} ions. It should be noted though that the isomer shift of the B lines is even smaller than the lower limit of the tetrahedrally co-ordinated Fe^{3+} ions, 0.2 mm/s,

and the quadrupole splitting of the B lines is also smaller than A lines. If the B lines were due to tetrahedrally co-ordinated Fe^{3+} ions, the quadrupole splitting would have been greater than those of A lines. Another possibility is that A component is due to metallic iron, which would also give rise to a vanishingly small isomer shift. The ratio of areas if A and B lines 1:1.25, is proportional to the number of iron atoms of each type. This would imply that 56% of the Fe present in the sample is metallic iron and other 44% corresponds to octahedrally co-ordinated Fe^{3+} ions. These results agree very well with the EXAFS results where it was found that first nearest neighbor shells of Fe atoms were composed of 6 oxygen and 8 Fe atoms. From the pre-edge feature analysis, which will discuss in chapter 5, we can eliminate the possible existence of tetrahedrally co-ordinated Fe^{3+} ions and found that 40% of the Fe atoms in the sample were surrounded by oxygen atoms while the other 60% were metallic iron. We can therefore conclude that these two configuration deduced from the EXAFS measurements give rise to the A and B components respectively , observed in the Mossbauer Data. The Mossbauer spectra of Fe in PVG consolidated to 1200^{0}C is shown in Figure 3.7.4. From the Figure it can be seen that consolidation of the higher Fe concentration sample to 1200^{0}C gives rise to internal magnetic fields. The spectra was best fit by two six line spectra corresponding to two magnetic hyperfine fields,

B=370 KG and B=425 KG, are close to 330 and 515 KG the magnetic hyperfine fields of Fe and Fe_2O_3 respectively[23]. The ratio of intensity of the two components, 1.3 is similar to that measured previously between two quadrupole splittings at 650°C. This again confirm the assignments of the two iron products formed in the glass. Small deviations from the pure component values can easily be explained by the effect of the silica bond and inhomogeneities in composition of the random porous glass medium. The magnetic hyperfine fields were observed only in the high concentration samples after consolidation. When PVG is impregnated with $Fe(CO)_5$ the vapors penetrate into all the pores uniformly as shown in figure 2.1. Photolysis decomposes the $Fe(CO)_5$ and binding some Fe atoms to the glass surface. These atoms then nucleate the formation of large clusters which are trapped within the pore. and photolysis binds the Fe compound into the pore surface.

3.8. Mossbauer studies of Fe in glass gels:

Glass gels were impregnated with iron pentacarbonyl the same as that of PVG. Then the gels were irradiated with 30 nm UV light which binds the Fe on the surface of gel.

Mossbauer spectra of Fe impregnated in glass gels and heated to 650^{0}C and 1200^{0}C are shown in Figure 3.8.1 and 3.8.2 respectively. The hyperfine parameters obtained using least square fitting results are listed in table 3.4. Samples heated to 650^{0}C can fit with two Lorentzians or one quadrupole doublet. The isomer shift and quadrupole splitting values are consistent with octahedrally co-ordinated Fe^{3+} ions. The Mossbauer spectrum of Fe gel which is heated to 1200^{0}C can best be fit with two quadrupole doublets and from the isomer shifts and quadrupole split values we can identify them as due to tetrahedrally and octahedrally coordinated Fe^{3+} ions. Widths of Lorentzians has increased as compare to the width of the lines at 650^{0}C indicating that there is a broader distribution of hyperfine parameters. From the areas of A and B lines we can determined that approximately 23% of Fe is in tetrahedral coordination.

Table 3.4. Mossbauer parameters of Fe photodeposited in glass gels.

Sample	I.S.* mm/s	Q.S. mm/s	Width
Heated to 650^{0}C	0.40	0.95	0.36 mm/s
Heated to 1200^{0}C	A. 0.23 B. 0.42	2.0 0.67	0.49 mm/s

* Isomer shift relative to center of α-Fe spectrum.

3.9. Summary:

The photolysis process binds the iron carbonyl to glass surface. In PVG Fe exists at two different sites as elemental iron and octahedrally co-ordinated Fe^{3+} ions. Heating to 650^0 or cooling down to 77K does not change the state of Fe atoms. But after the glass was consolidated by heating to 1200^{0}C room temperature Mossbauer spectrum shows magnetic hyperfine splitting. The corresponding hyperfine fields were 370 and 425 kG. The size of the Fe particles increases with annealing temperature. In glass gels after heating to 650^{0}C Fe exists in a single site as octahedrally co-ordinated Fe^{3+} ions. But after heating to 1200^{0}C part of the iron ions become tetrahedrally coordinated.

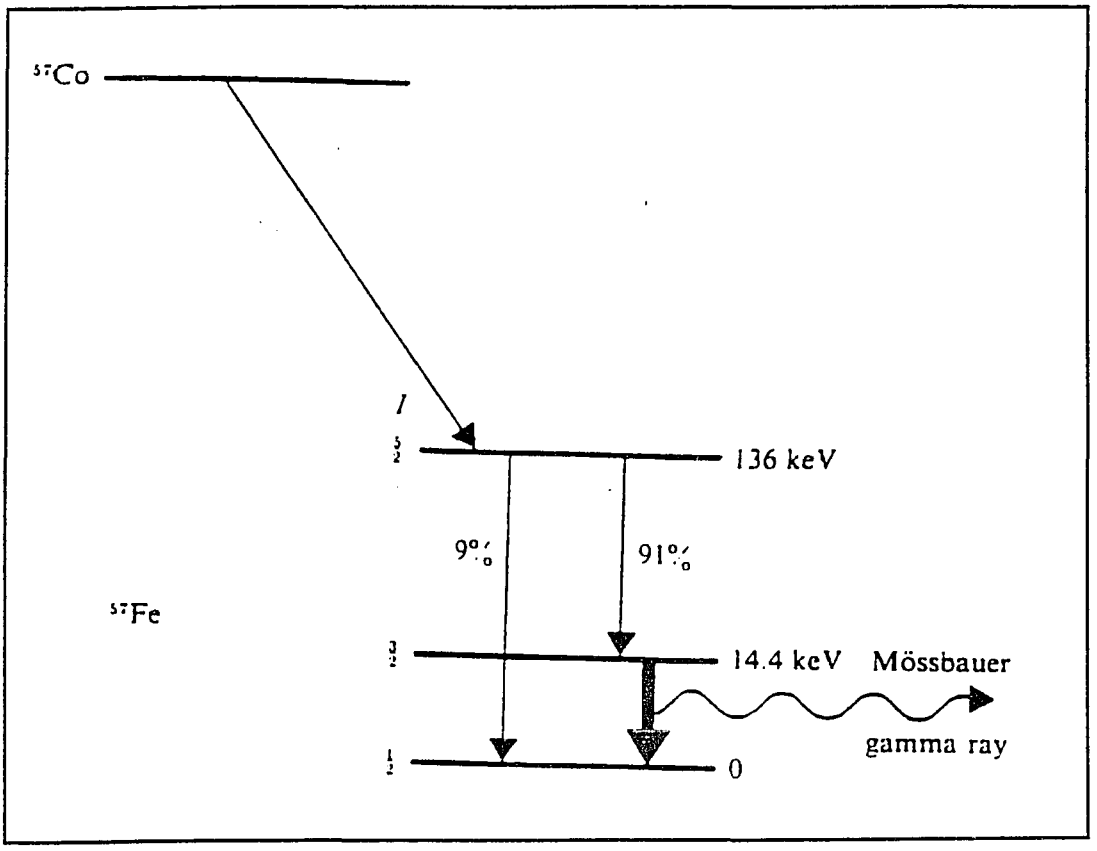

Figure 3.1.1. Decay scheme of ^{57}Co.

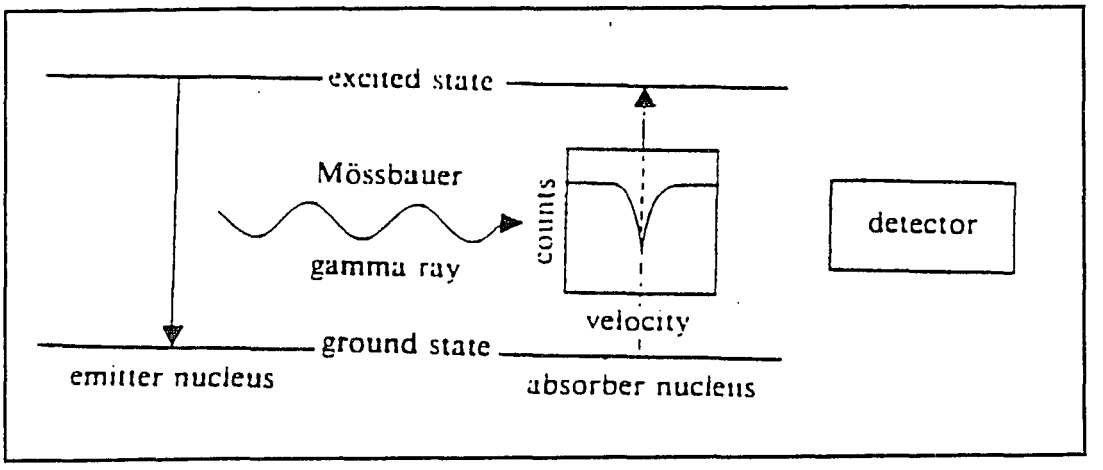

Figure 3.2.1. A schematic representation of Mossbauer spectroscopy.

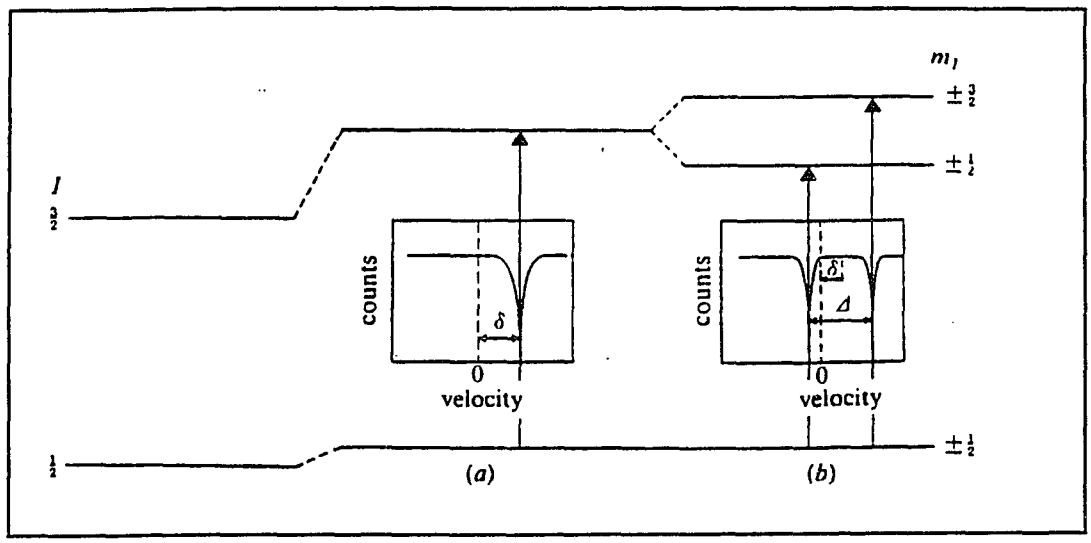

Figure 3.3.1. The effects on the nuclear energy levels of ^{57}Fe due to isomer shift and quadrupole splitting.

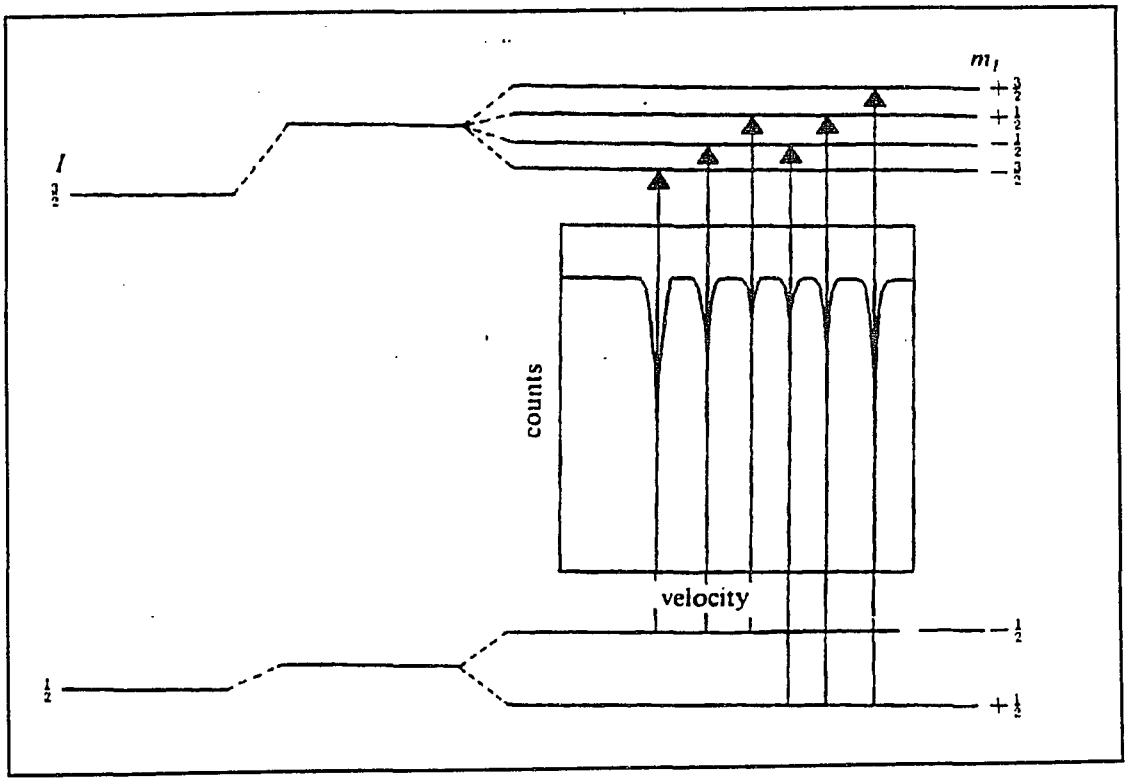

Figure 3.3.2. The effect of magnetic splitting on the energy levels of ^{57}Fe.

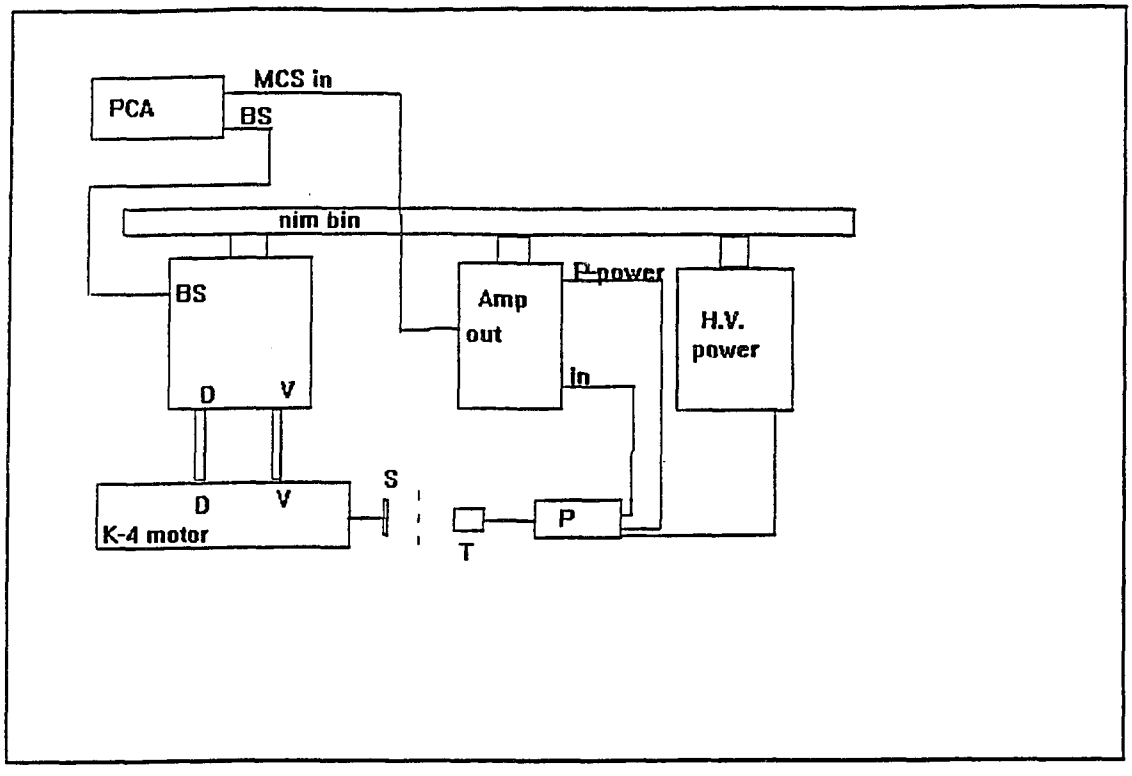

Figure 3.5.1. Block diagram of Mossbauer spectrometer.

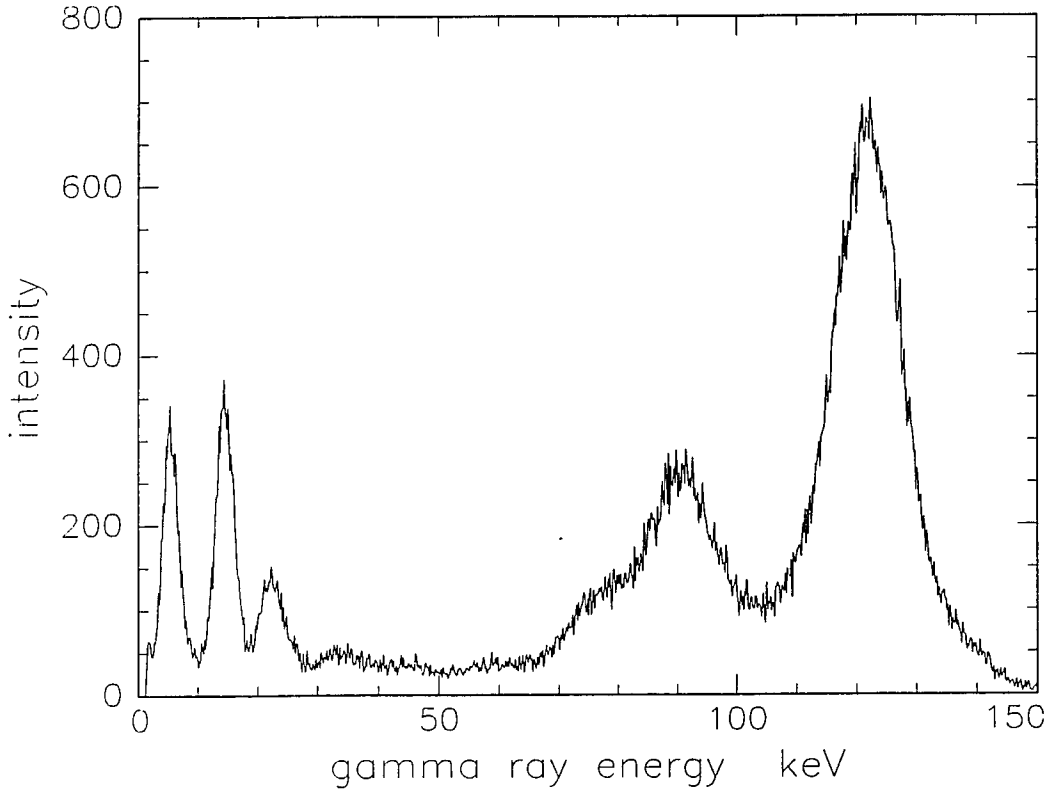

Figure 3.5.2. Energy spectrum of ^{57}Co.

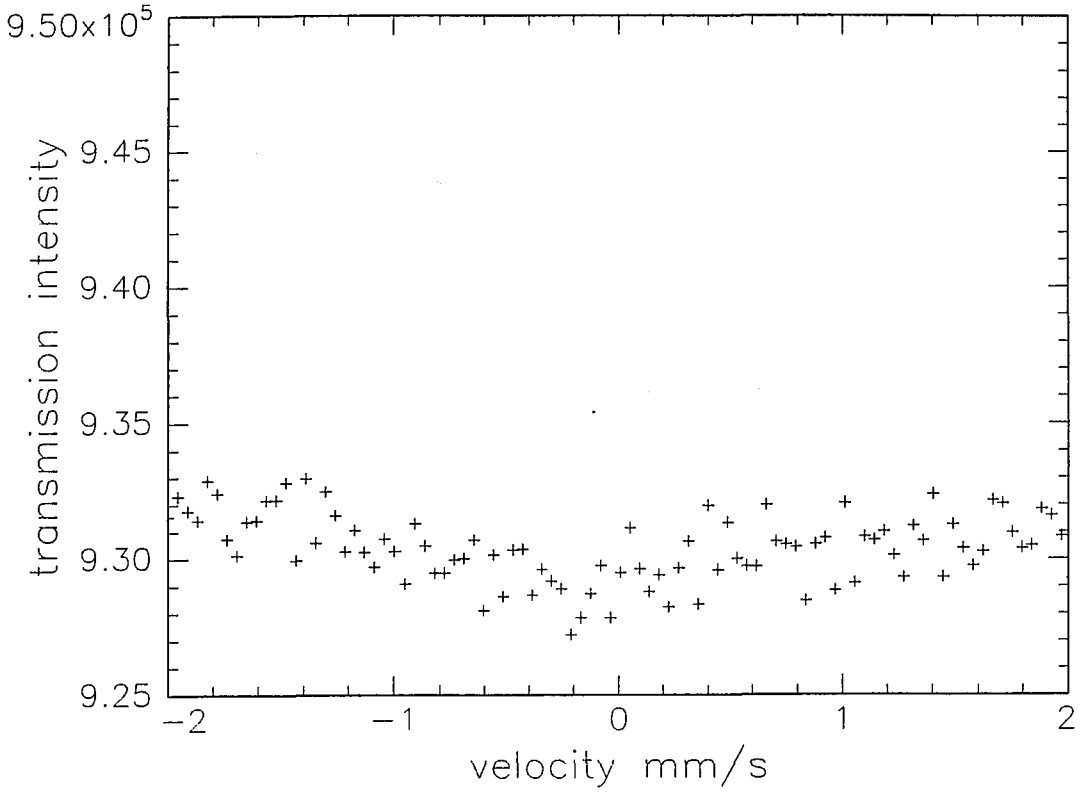

Figure 3.7.1. Mossbauer spectrum of unphotolyzed PVG.

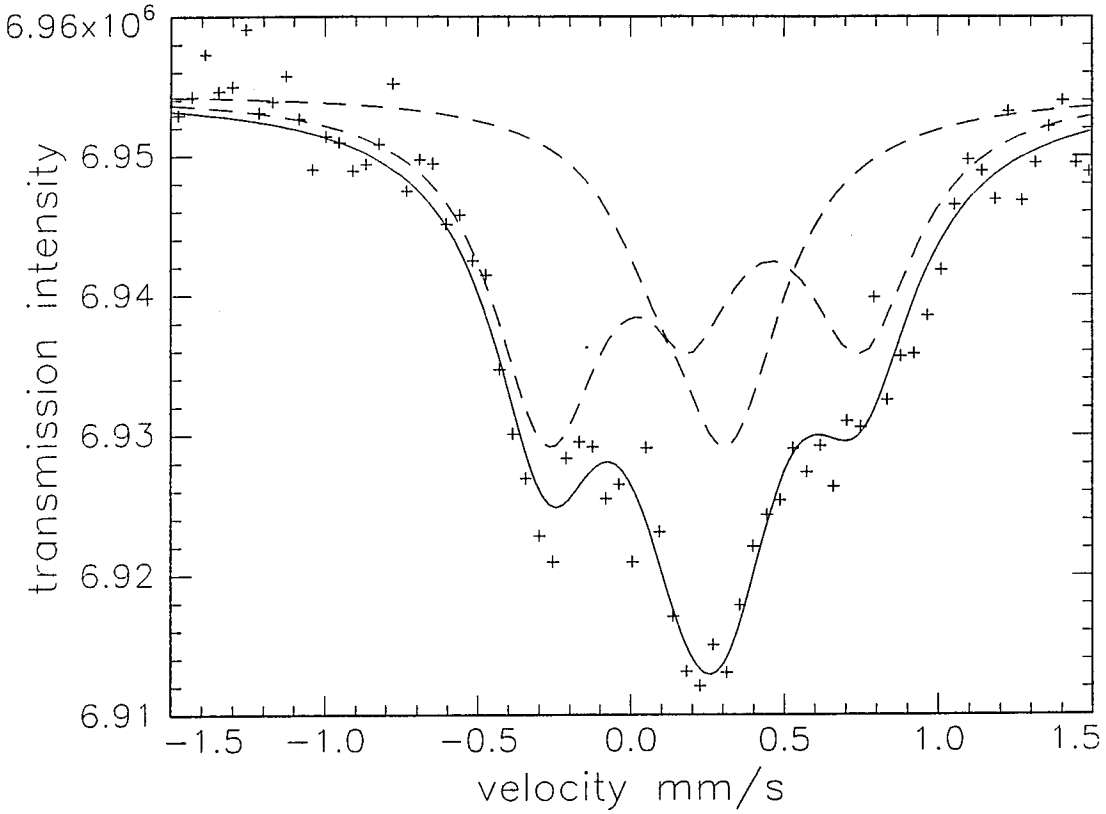

Figure 3.7.2 Mossbauer spectrum of unheated PVG.

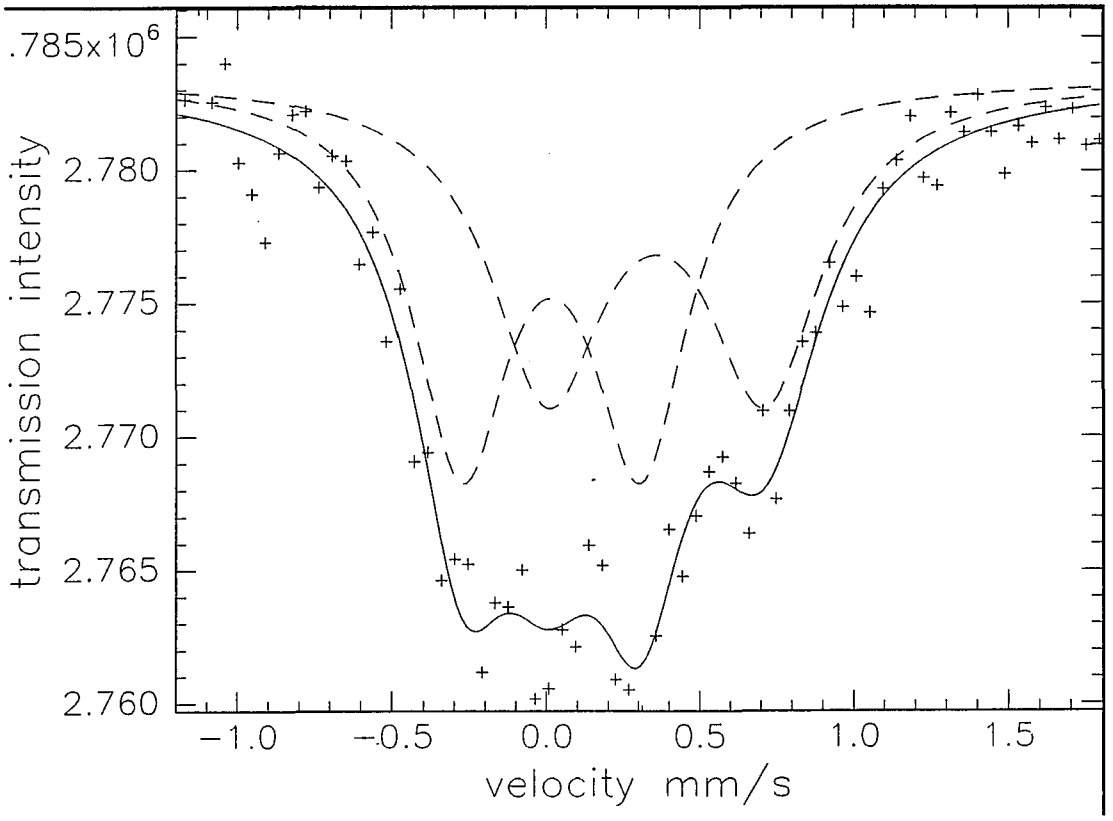

Figure 3.7.3 Mossbauer spectrum of PVG heated to 650°C.

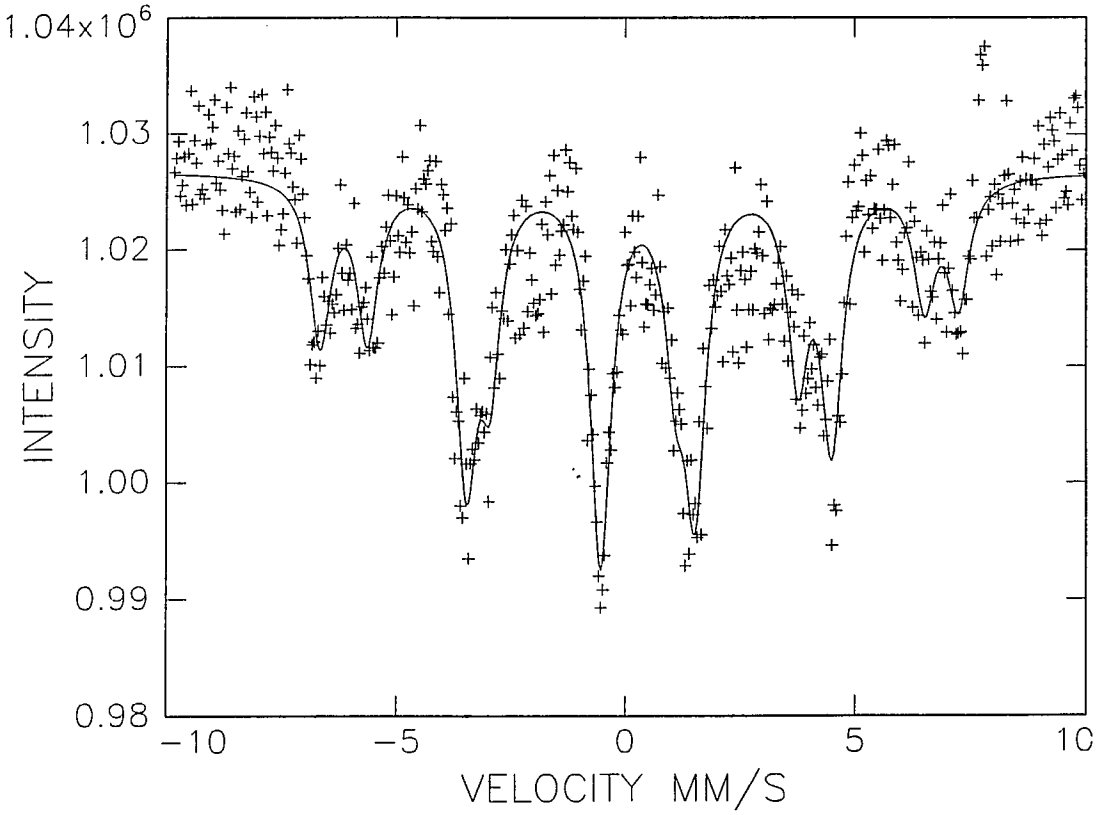

Figure 3.7.4 Mossbauer spectrum of PVG heated to 1200°C.

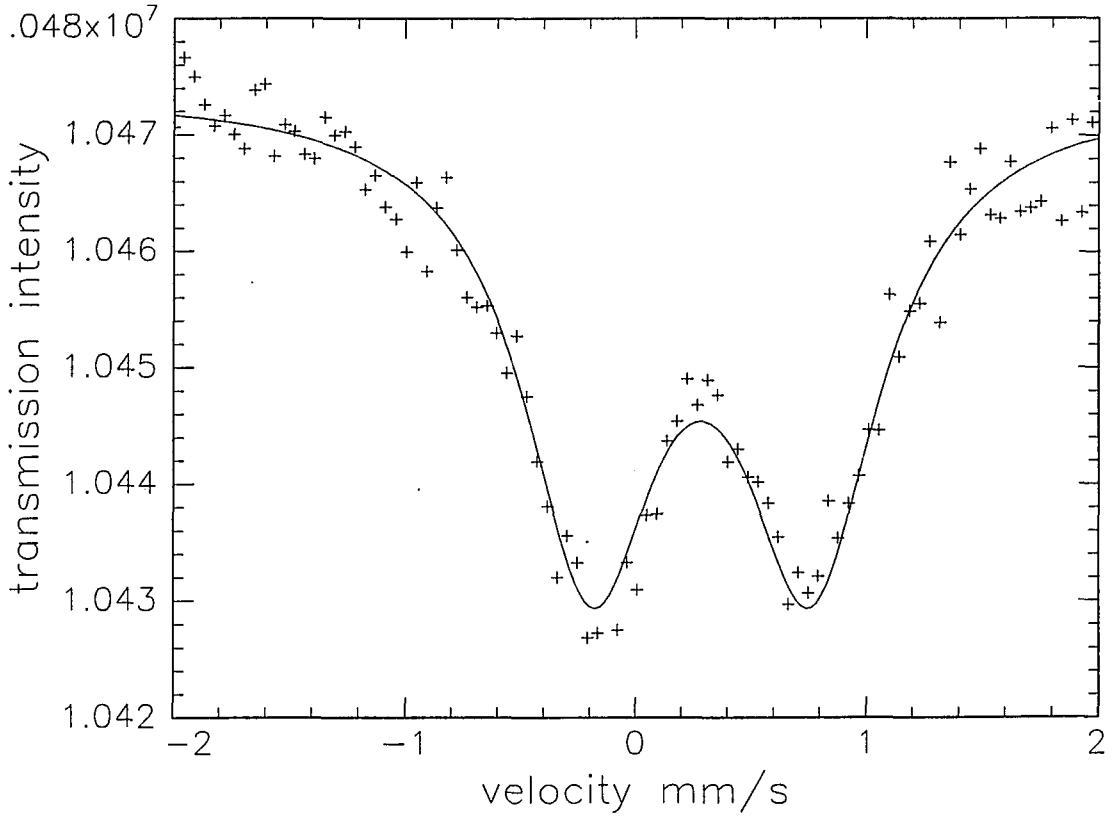

Figure 3.8.1. Mossbauer spectrum of Fe in gel heated to 650°C.

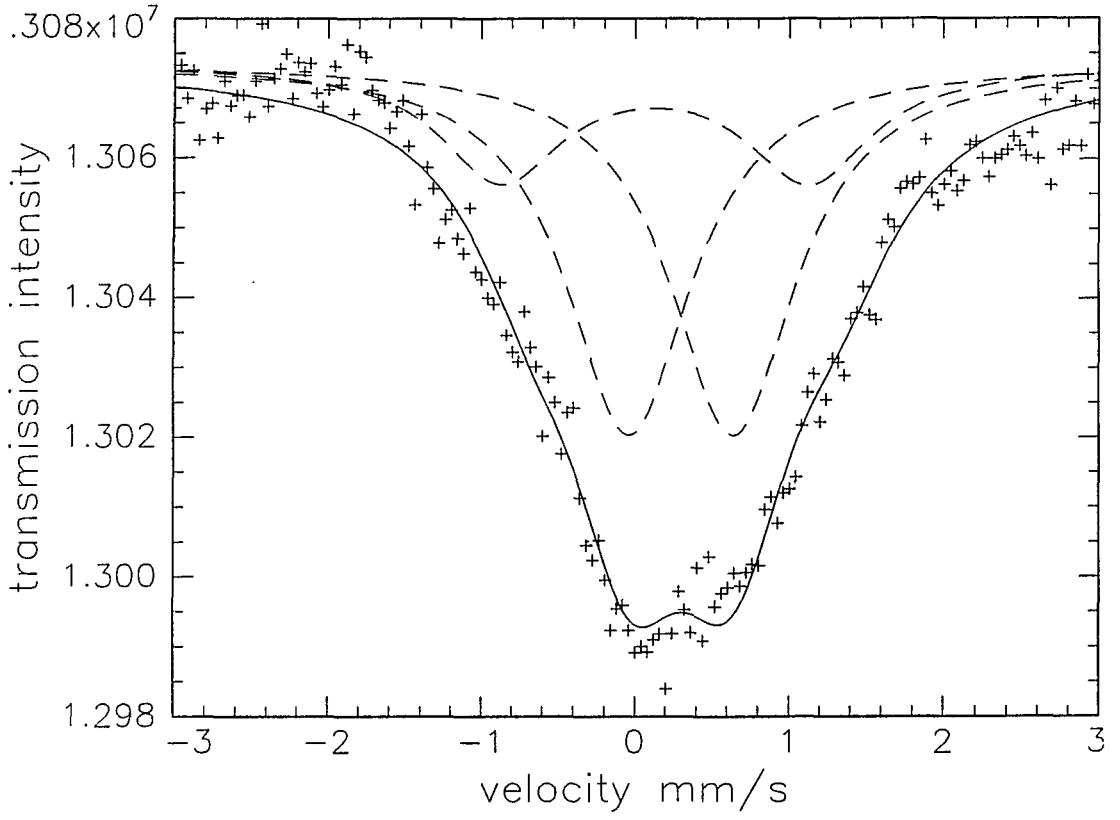

Figure 3.8.2. Mossbauer spectrum of Fe in gel heated to 1200°C.

CHAPTER 4.

Extended X-ray Absorption Fine Structure:

4.1. Introduction:

The Extended X-ray Absorption Fine Structure(EXAFS) is the small amplitude oscillations in absorption coefficient about 30 eV above the absorption edge and typically extending 1000 eV further as shown in Figure 4.1.1 for the K-edge of Fe in PVG heated to 650^{0}C. By studying the EXAFS spectra one can determine the structural parameters such as interatomic spacings, co-ordinating numbers, amplitude of thermal oscillations type of neighboring atoms of an atom of specified Z. Characteristics of EXAFS are determine by local environment of atoms, and are insensitive to the presence or absence of long range order of the system. Therefore it is well suited for the study of structure of glassy materials.

4.2. Basic theory:

Consider a beam of photons with intensity I travelling in a homogeneous absorbing medium(Figure 4.2.1). Due to absorption the beam intensity decreases as the path length

x increases with exponential law as $I=I_0e^{-\mu x}$ where I_0 is the intensity at x=0. The absorption coefficient μ is a function of photon energy. Photons of different energies are absorbed differently by the medium. X-rays are absorbed by matter primarily through the photoelectric effect. This occurs when a bound electron is excited to a continuum state by an incident photon of energy $h\nu$ (Figure 4.2.2). Then the final electron has kinetic energy $E_k=h\nu-E_0$. For photon energies less than E_k excitation is not possible. If one measures the absorption coefficient as a function of photon energy a sharp rise or edge is observed at K-shell threshold energy.

The structure of X-ray absorption spectrum from about 0 to 30 eV above the edge is known as X-ray Absorption Near Edge Structure(XANES). At these low energies the excited electronic states must be described in terms of detailed wave functions of solid. Only about 30 eV above the edge excited states can be considered as nearly free and their wave functions can be considered as spherical outgoing waves. As these free electron waves propagate through the solid, they undergo scattering at the near neighbor shells of atoms (Figure 4.2.3). These outgoing electron waves and backscattered electron waves can interfere destructively or constructively depending on the phase difference between them. Destructive and constructive interference implys a

reduction or an enhancement of the amplitude of the final state wave function in the region where it overlaps and hence the intensity. In the single scattering plane wave approximation, the normalized absorption *vs* wave vector spectrum[30], $\chi(k) = (\mu(k)-\mu_0)/\mu_0$, is given by

$$\chi(k) = \Sigma S_i(k)\ N_j\ F_j(k)\ \exp(-\sigma_j^2 k^2)\ \exp(-2r/\lambda)\ \mathrm{Sin}(2kr_j+\Phi_i+\Phi_j)/kr_j^2$$

where

$k = \{2m/\hbar^2(E-E_0)\}^{1/2}$, μ_0 is the absorption coefficient of the isolated atom , μ (k) is the absorption coefficient, k is the photoelectric wave vector, while E is the energy of incident photon, E_0 is the absorption threshold energy and m is the electron mass. N_j is the number of scattering atoms at a distance r_j from the absorber atom, $S_i(k)$ is the correction factor for absorber atom multi-electron effects, $F_j(k)$ is the backscattered electron amplitude function, and $\exp(-2\sigma_j^2 k^2)$ is the Debye-Waller factor which includes thermal and static disorder terms with root mean square displacement, σ_j. The term $\exp(-2\ r/\lambda)$ accounts for the loss of photo-electrons to inelastic processes, λ being the mean free path of the electrons, $\sin(2kr_j+\ \Phi_i+\Phi_j\ )$ is the phase interference term, Φ_i is the central atom phase shift and Φ_j is the phase shift for the j^{th} shell of neighboring atoms. Phase shifts and amplitude functions can be obtained from similar model compounds or can be

calculated from first principles.

4.3. Data analysis:

4.3.1. Edge normalization and background subtraction:

The analysis of EXAFS data begins with edge normalization. That is subtraction of part of the absorption spectrum due to other atoms of the sample and other electron shells of the absorbing atom. This is accomplished by fitting a function to the pre-edge region and extrapolating the fit over entire EXAFS range, and subtracting it from the data. In fluorescence mode the background absorption, μ_0, usually increases with increasing X-ray energy. This is due to increasing beam penetration of the sample, increased Compton scattering and reduced sample absorption for its own fluorescence. To accurately subtract the background absorption, μ_0, a smooth curve was fit to the absorption spectrum and then subtracted from the experimental data. The usual fits employed in this work are 3-region fits of order 3. After the background subtraction and edge normalization the $\chi(E)$ function is converted to k space with equation $k=\{2m/\hbar^2(E-E_0)\}^{1/2}$. The E_0 value

represents the zero energy point of the ejected photoelectric wave. In this work it is set to the mid edge height energy during the calculation of $\chi(k)$ function.

4.3.2. Fourier transform of $\chi(k)$ and curve fitting:

The normalized $\chi(k)$ function is weighted by multiplication by k^3. This factor cancels one power of k in the EXAFS equation and roughly compensates for the $1/k^2$ behavior of F(k) at large values of k. It has the effect of weighing the EXAFS oscillations more or less uniformly over the entire range. Fourier transformation of the data separate out the contributions of the different shells of atoms around the absorber atom and yield the Radial Distribution Function(RDF). The peak positions of this EXAFS derived RDF differs from actual values due to phase shift functions. Although the Fourier transform peaks do not coincide with the actual absorber backscatter distances, one can approximate the correct distances by comparing the Fourier transform of model compounds with the same type of backscattering atoms. For this we have to assume the type of backscattering atoms or need information of type of

backscattering atoms from another method. The determination of accurate distances from the EXAFS thus requires peak fitting in addition to the Fourier transform. A convenient analysis method is that of Fourier filtering followed by curve fitting of the EXAFS oscillations from a single shell of backscatters. In order to do this, part of RDF containing information for a single shell is back transformed into k space. The back transform resembles the initial EXAFS $\chi(k)$ function except that it contains only frequency information from one shell of atoms. The back transformed single shell EXAFS oscillations fit with model expression such as equation (1) to find the optimum values for parameters. The $S(k)$ and $\lambda(k)$ terms assumed to be constants over the k range studied(3.8-11)$Å^{-1}$. Model compounds of known structure, Fe and Fe_2O_3 were processed first in order to find the best fit value for the term S. In fits of these models all adjustable parameters were allowed to vary except the coordination number and distance of the particular shell of atoms. Theoretical curves calculated by Teo and Lee[31] were used for backscattering amplitudes and phase shift functions in all calculations.

4.4. Results and discussion:

All EXAFS data were collected in the fluorescence mode, which is well suited to study the impregnated Fe samples since the Fe concentration is very low and the samples are

relatively thick. Figures 4.4.3-4.4.6 a,b,c,d show the calibrated and averaged absorption spectrum, background subtracted and normalized χ function, the structure function, and the curve-fitted back-transform of the first peak of RDF of Fe in Fe_2O_3, PVG/unheated, PVG/heated to 650°C, PVG/heated to 1200°C respectively. Since heat treatments of glasses were carried out in air, the most obvious iron product in glass is one form of iron oxide. Therefore first data were tried to fit the back-transformed data to one shell of oxygen atoms. The best fit can be obtained using a single shell of oxygen atoms for one of the glass samples is shown in Figure 4.4.5. All other samples gave similar fits. Second, assuming the iron product is a compound like γ-Fe_2O_3 with tetrahedrally and octahedrally co-ordinated iron ions, a fit of the data with two Fe-O distances was tried. But two distances converge to one and the final fit is similar to Figure 4.4.5. All samples were tried with silicon atoms as nearest neighbors but none of the models agree with the data. All samples gave very good fits if we assumed that the first peak of the RDF was due to two separate components, an iron oxide whose nearest neighbor shell is composed of oxygen atoms and elemental Fe surrounded only by other Fe atoms. Since the EXAFS spectra derives from Fe in two separate compounds, the $\chi(k)$ function was assumed to be a linear combination of the individual EXAFS functions of the elemental Fe and iron oxide

components, $\chi_{Fe\text{-}Fe}(k)$ and $\chi_{Fe\text{-}O}(k)$;

$$\chi(k) = a\chi_{Fe\text{-}Fe}(k) + b\chi_{Fe\text{-}O}(k).$$

The fraction of the two components in the glass, a and b, were assumed to be 0.56 and 0.44 as previously determined from the Mossbauer spectra. The second peak of the RDF in all the samples can be modeled with only Fe atoms. But in the sample that is heated 1200°C Fe-Fe distances are slightly different in the two components. Other samples show only one Fe-Fe distance corresponding to the same Fe-Fe distance in both components. The number of atoms cannot be determined accurately because of the large correlation of σ^2 parameter and coordination number. On the other hand all parameters derived from EXAFS for the second shell of atoms are not accurate due multiple scattering. That is electron waves scattered from the second shell of atoms can be scattered again from the first shell before arriving at the central atom resulting different phase shift and amplitude values and hence causing errors in fitting parameters. The bond distance, number, and type of near neighbor atoms yielding the minimum χ^2 value for each compound are listed in tables 4.1 and 4.2.

Table 4.1 -EXAFS results of Fe-O compound. R=radial distance, N=number of atoms.

sample	First shell(oxygen)		Second shell(iron)	
	R(Å)	N	R(Å)	N
1a	1.79	6.8	2.86	6.9
1b	1.81	6.6	2.98	4.0
1c	1.84	6.7	3.0	3.6
2a	1.77	7.4	2.86	4.0
2b	1.80	6.9	2.98	3.2

1-High concentration of Fe.

2-Low concentration of Fe.

a-Sample heated to 1200^{0}C.

b-Sample heated to 650^{0}C.

c-Unheated sample.

Table 4.2 -EXAFS results of Fe-Fe compound. R=radial distance, N=number of atoms.

sample	First shell(iron)		Second shell(iron)	
	R(Å)	N	R(Å)	N
1a	1.97	7.7	3.03	13.3
1b	1.98	7.8	2.98	3.9
1c	1.84	6.7	3.0	3.6
2a	1.99	7.6	2.86	8.1
2b	1.99	8.7	2.98	3.2

From the tables 4.1 and 4.2 several conclusions can be drawn about the first shell. First the measured Fe-O or Fe-Fe distances vary less than 1% between samples heated to 650^{0}C and consolidated to 1200^{0}C. Second the type and number of nearest neighbors is independent of annealing temperature and varies slightly with initial loading. In addition to the Fe-O and Fe-Fe structures considered above, another calculation was done assuming part of the Fe was surrounded by shell of silicon atoms. The fits are noticeably worse if we take the Fe-Si compound to be greater than 30%. The Fe-Fe distance observed, 2Å, is intermediate between that of

bulk α-Fe(2.48Å) and the typical distance, 1.8Å, observed in the amorphous Fe metallic glasses[32], $Fe_{81}B_{13.5}Si_{3.5}C_2$, and $Fe_{80}B_{15}Si_3C_2$. The large shrinkage in bond length is attributed to an increase in covalent character of the bonds due to the non-metallic C, B, and Si impurities[32,33].

4.5. Summary:

EXAFS results agrees with the two compound model. That is, immediately after photolysis two types of iron compounds has formed. One with oxygen as nearest neighbors and the other as Fe nearest neighbors to iron. Heating of the samples either to 650°C or 1200°C does not affect to the composition of Fe particles in the glass. There is no significant change in the percentage of iron oxide compound even after heating to 650°C or 1200°C. The Fe-O and Fe-Fe nearest neighbor distances of two compounds are 1.8Å and 2Å respectively.

4.6. EXAFS studies of Fe in glass gels:

X-ray absorption spectra of glass gels impregnated with Fe were collected using Synchrotron radiation and analyzed following the same procedure as in PVG which is described earlier. Figures 4.4.5-4.4.6 a-c show the X-ray absorption spectra, back ground subtracted χ(k) function, and Radial Distribution Functions(RDF) derived from EXAFS analysis, of Fe impregnated in gels heated to 650°C and 1200°C,

respectively. The first peak of RDF in Figure.4.4.5c can be fit (Figure 4.4.5d) with a single shell of six oxygen atoms at a distance of 1.82 Å. This agrees with the Mossbauer results in which we show one quadrupole doublet corresponding to octahedrally coordinated Fe^{3+} ions. In consolidated gel the first back transformed peak of RDF in Fig 4.4.67c can be fit with two shells of 5.8 and 3.6 oxygen atoms at distance of 1.90 Å and 1.70 Å respectively. This also agrees with the Mossbauer results where we identified the two doublets as due to tetrahedrally and octahedrally coordinated Fe^{3+} ions.

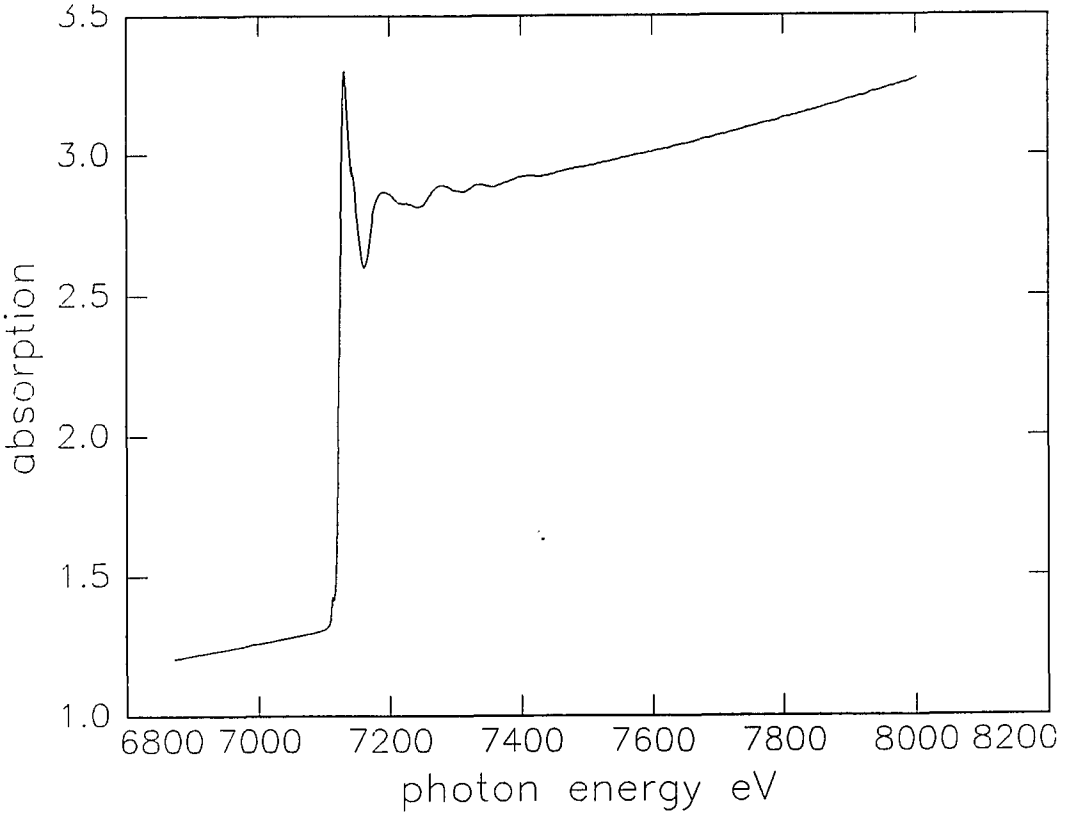

Figure 4.1.1. X-ray absorption spectrum of PVG heated to 1200^{0}C.

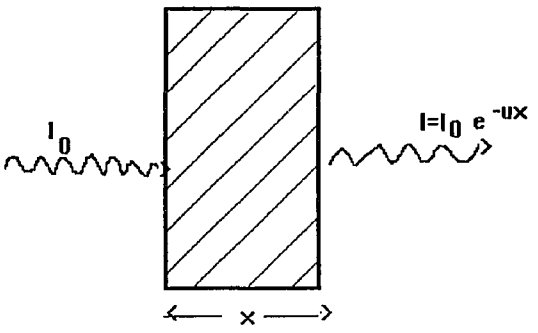

Figure 4.2.1. Attenuation of x-rays as they pass through a material of thickness x.

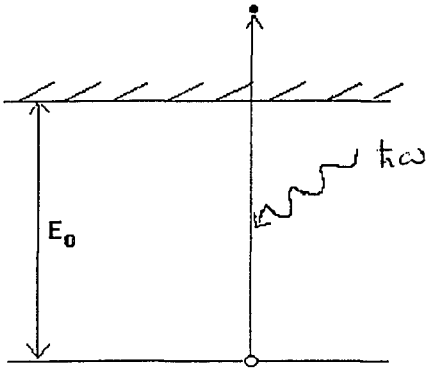

Figure 4.2.2. Schematic representation of the transition from a core state with binding energy E_o to a state with a hole left behind and a photoelectron with energy $\hbar\omega$-E_o.

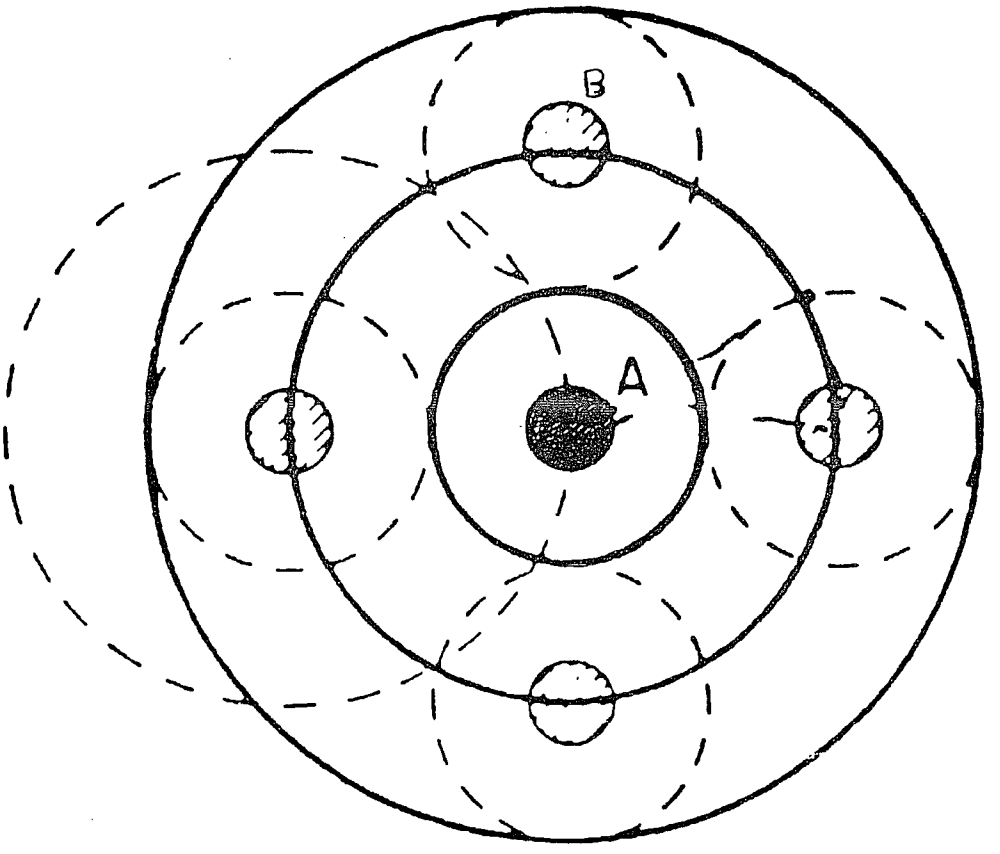

Figure 4.2.3. Interference of outgoing photoelectron waves and backscattered electron waves.

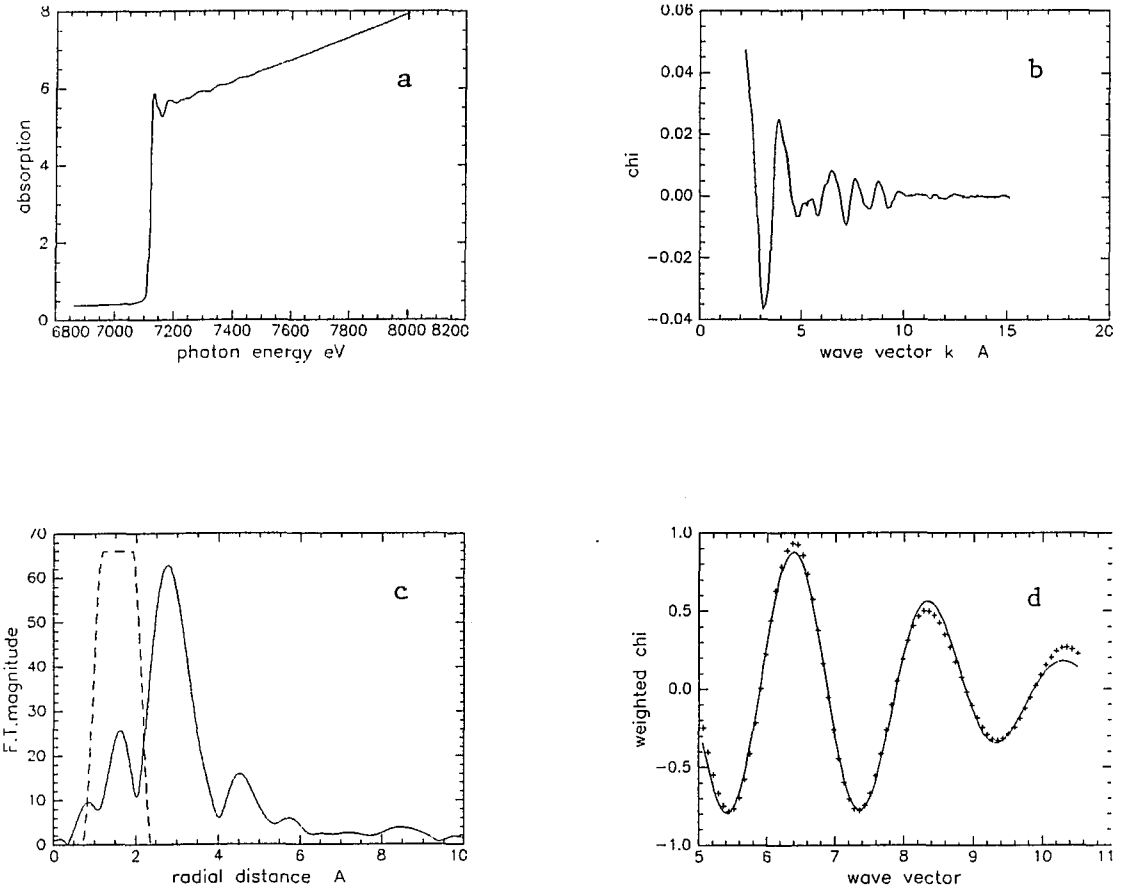

Figure 4.4.1. EXAFS data reduction steps of Fe_2O_3.

a)X-ray absorption spectrum.

b)Background subtracted χ function.

c)Radial distribution function.

d)Backtransformed first peak of RDF and one oxygen shell fit.

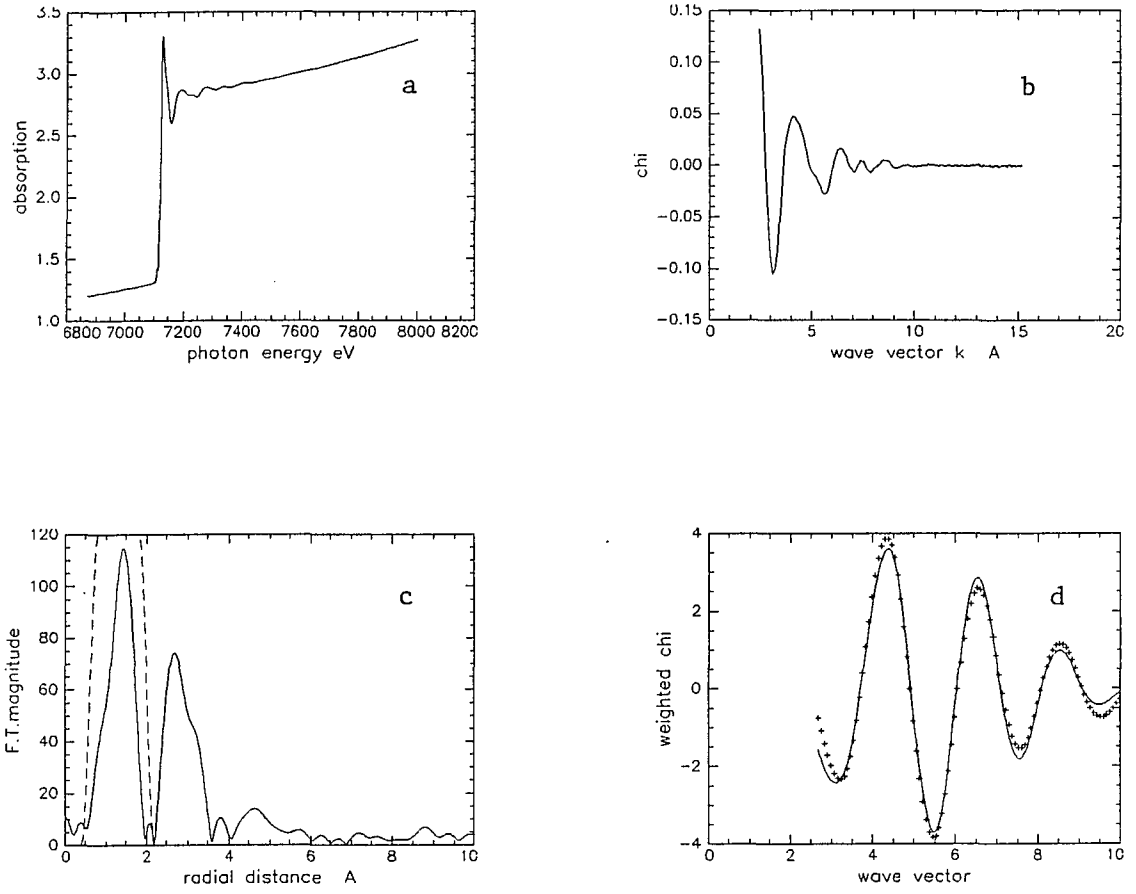

Figure 4.4.2. EXAFS data reduction steps of Fe in PVG heated to 1200^0C.

a)X-ray absorption spectrum.

b)Background subtracted χ function.

c)Radial distribution function.

d)Backtransformed first peak of RDF and one oxygen shell fit.

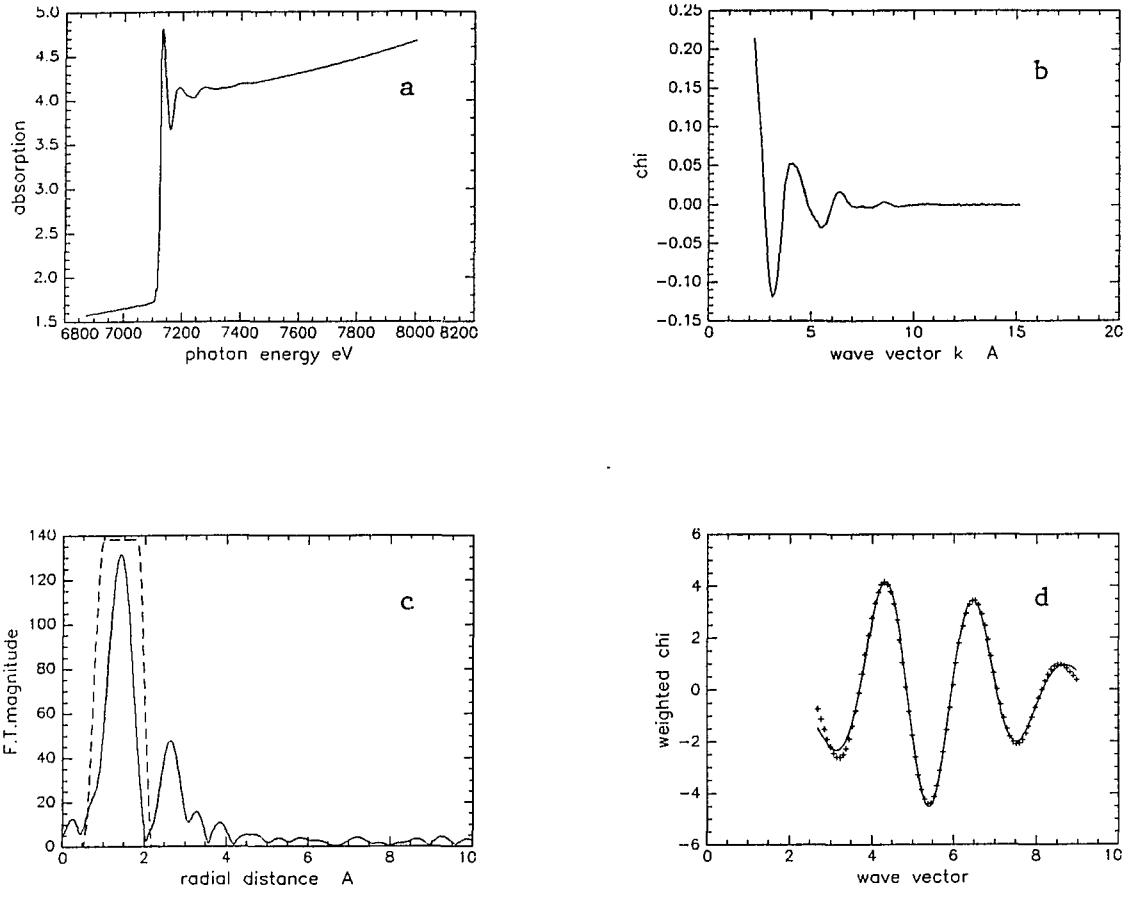

Figure 4.4.3. EXAFS data reduction steps of Fe in PVG heated to 650^0C.

a)X-ray absorption spectrum.

b)Background subtracted χ function.

c)Radial distribution function.

d)Backtransformed first peak of RDF and one oxygen shell fit.

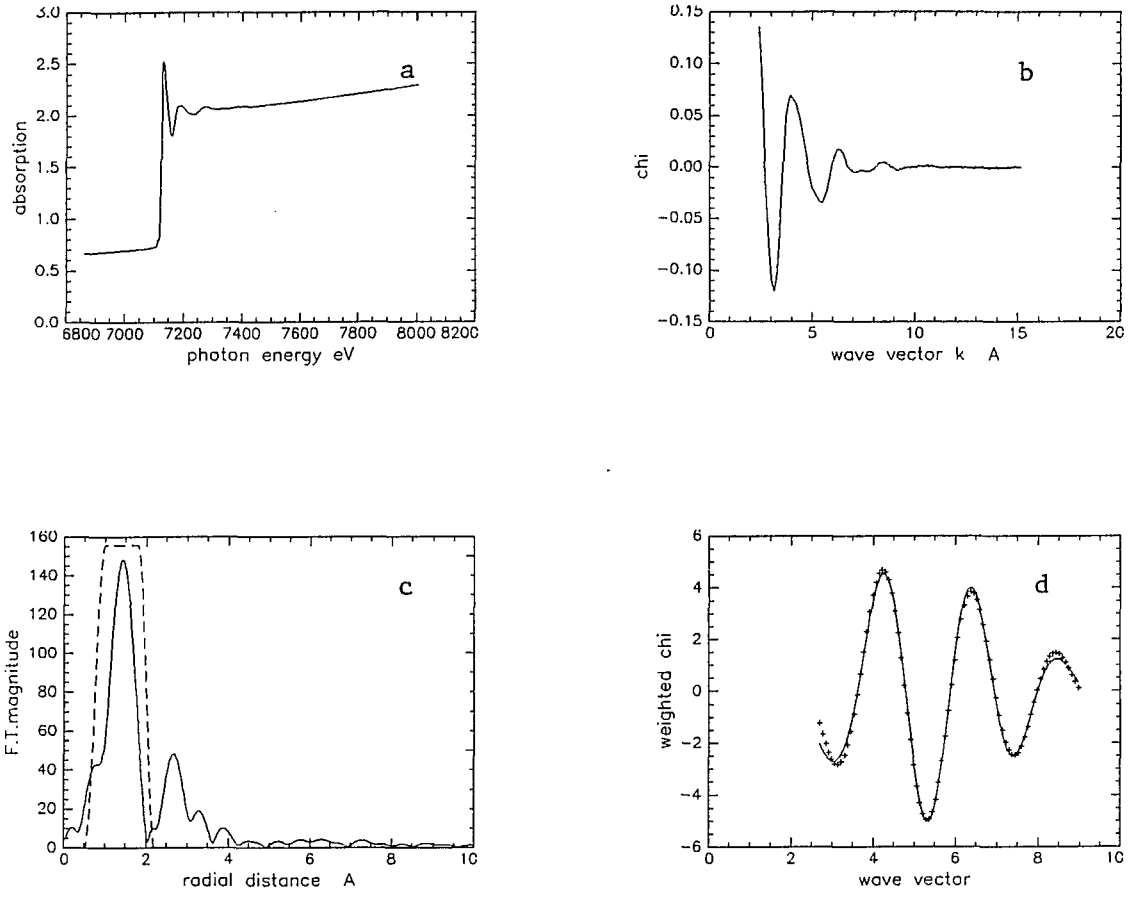

Figure 4.4.4. EXAFS data reduction steps of Fe in PVG unheated.

a)X-ray absorption spectrum.

b)Background subtracted χ function.

c)Radial distribution function.

d)Backtransformed first peak of RDF and one oxygen shell fit.

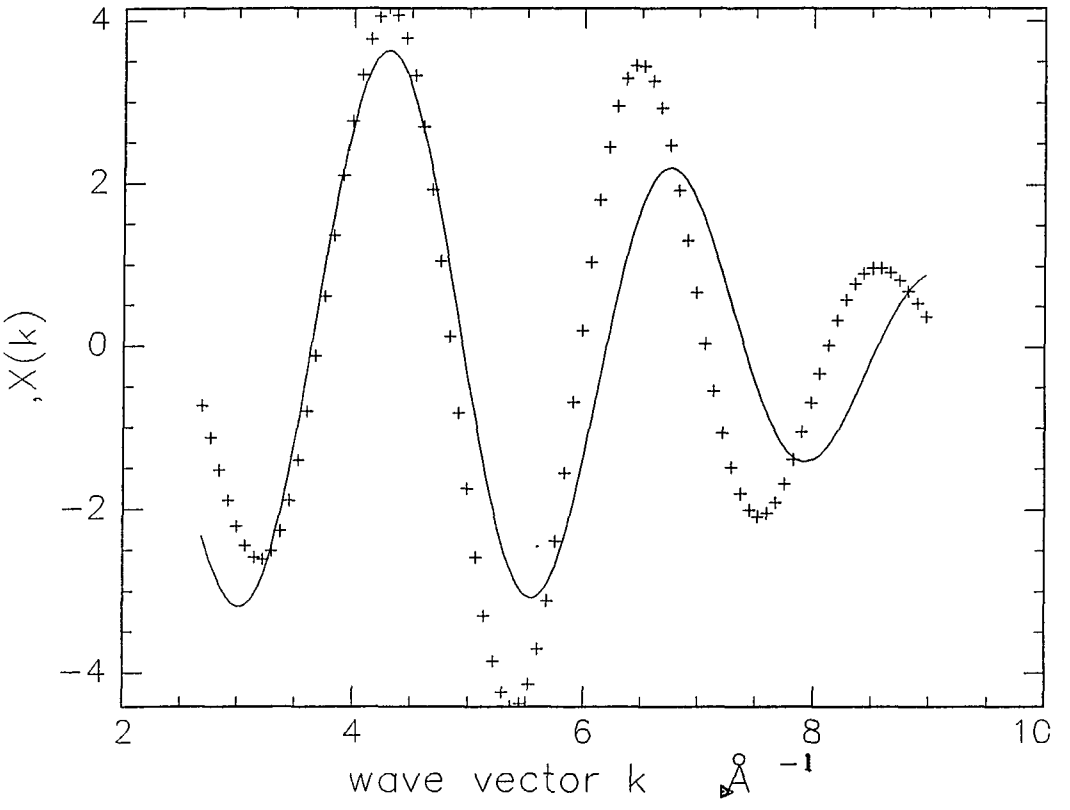

Figure 4.4.5. Back transform first shell data of Fe in PVG (+++) and one shell of oxygen fit (--).

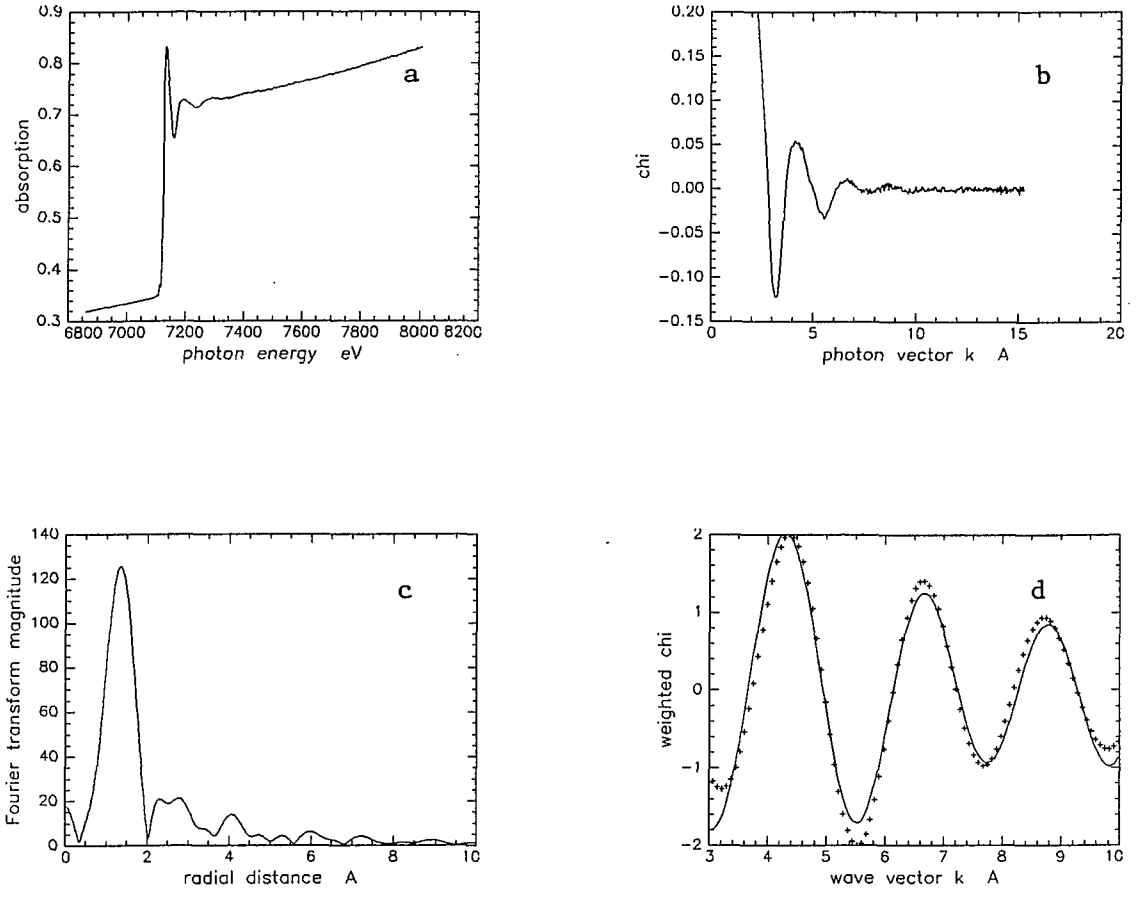

Figure 4.4.6. EXAFS data reduction steps of Fe in glass gel heated to 650^{0}C.

a)X-ray absorption spectrum.

b)Background subtracted χ function.

c)Radial distribution function.

d)++++ Back transformed first peak of RDF.

--- one oxygen shell fit.

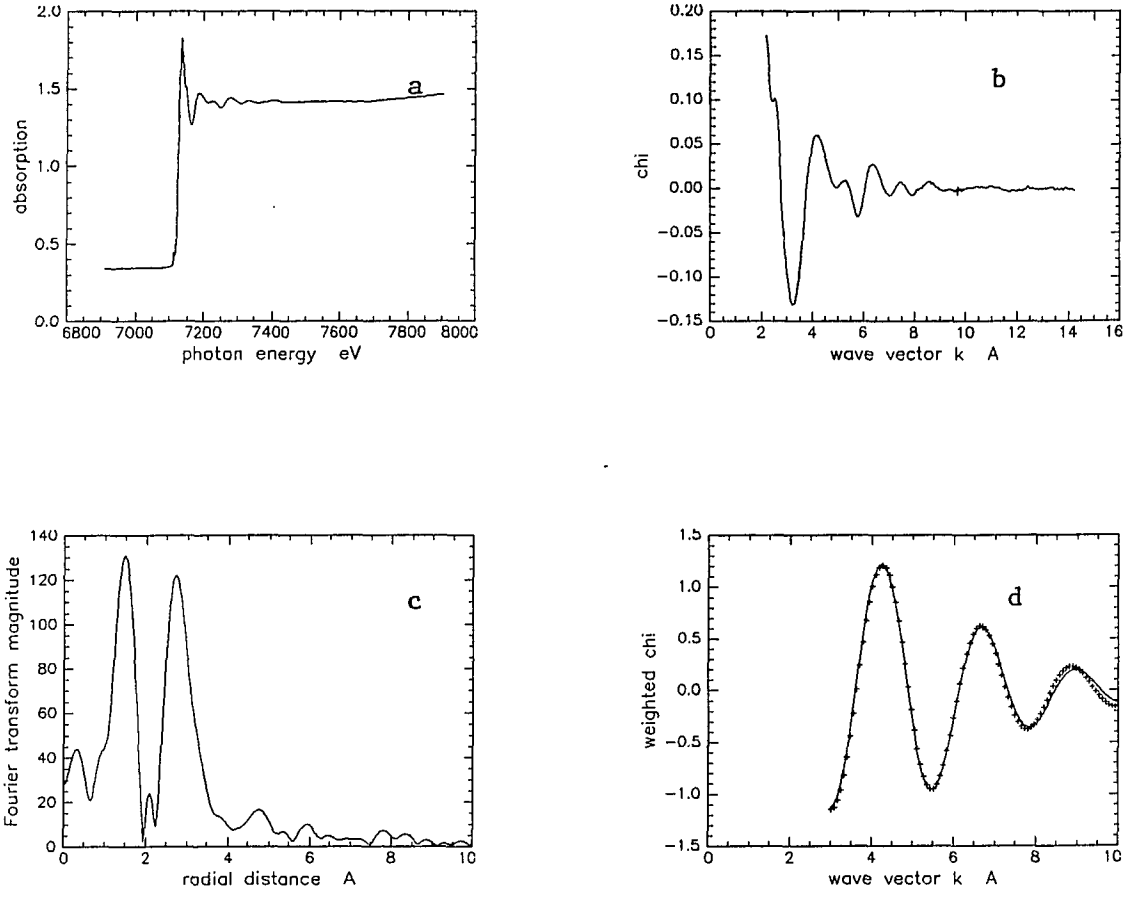

Figure 4.4.7. EXAFS data reduction steps of Fe in glass gel heated to 1200^{0}C.

a)X-ray absorption spectrum.

b)Background subtracted χ function.

c)Radial distribution function.

d)++++ Back transformed first peak of RDF.

--- two oxygen shells fit.

CHAPTER 5.

"Pre-edge" feature analysis.

5.1. Review of previous studies of "pre-edge" feature.

K-edge X-ray absorption of transition elements shows small peak below the absorption edge(Figure 4.1.1). This peak is associated with electronic transitions from 1s to 3d levels[34]. This transition is forbidden by dipole selection rules, but become allowed when there is some hybridization of Fe 3d orbitals and O 2p states. Previous studies of the pre-edge feature show that the intensity and energy(position) of the pre-edge peak vary in the most clearly systematic fashion with ion site symmetry, metal-legend bond type and metal ion valence[34-43]. For example Shulman et al[44] noted about a seven times increase of pre-edge intensity of tetrahedral Fe^{3+} compounds over octahedral Fe^{3+} compounds. Similarly Waychunas[45] reported an order of magnitude increase in this feature in tetrahedral Fe^{2+} as compared to that observed in octahedral Fe^{2+} compounds. Variations in valence state have a large effect on the energy of the pre-edge feature. A shift of about 2-3 eV upward shift is typically observed with each increase in the oxidation state by one valence unit[37,38]. The change of intensity can be explained from the site symmetry. Since

both 1s and 3d states are centrosymmetric, the transition probability should be small. When the iron site is non-centrosymmetric, a mixing of p and d orbital character occurs which intensifies the transition. The intensity is therefore large for regular tetrahedral than octahedral co-ordination. The energy shift due to valence change is mainly an electrostatic effect due to the increased binding energy of the 1s electron as the formal valence increases[46]. It has also been found that the character of ligands influences the effective charge on the metal iron. Hence compounds with Fe ions of the same charge state can demonstrate a edge shift depending on the effective charge around the Fe ion[47,48,49].

5.2. Data analysis, results and discussion:

Figures 5.2.1-5.2.4 a show the X-ray absorption near edge spectra of Fe_2O_3, Fe in PVG heated to 1200^{0}C, Fe in PVG heated to 650^{0}C, and Fe in unheated PVG respectively. In order to isolate pre-edge from the main edge, arctan functions were fitted to the main edges (Figures 5.2.1-4b) and subtracted from the experimental data. Then subtracted pre-edges were fitted using Lorentzian functions and finally normalized to the height of the edge crest. Energies and intensities of normalized pre-edges of α-Fe_2O_3 and Fe in PVG are shown in Table 5.1.

Table 5.1: Pre-edge positions and intensities of α-Fe_2O_3 and Fe in PVG.

Sample	Annealing temp.	Energy(eV)	Normalized intensity
α-Fe_2O_3	Room temperature	7114	0.034
1a	1200^0C	7113	0.016
1b	650^0C	7113	0.014
1c	Room temperature	7113	0.012

From the table 5.1 and figure 5.2.5 it can be seen that the energy of pre-edges of Fe in PVG is the same in all glass samples and is almost the same as that of Fe_2O_3 indicates that the oxidation state of Fe-O compound of Fe in PVG is Fe^{3+}. The difference of pre-edge position, 1 eV, of Fe_2O_3 and Fe in glass is about the energy resolution of the monochromator and may be due to difference in chemical environment. The intensities of peaks of Fe in PVG are more than 50% less than the peak intensity of Fe_2O_3. In the case

of α-Fe_2O_3 all the Fe atoms are octahedrally surrounded by six oxygen atoms. Therefore this compound has the lowest contribution to the pre-edge compared to all other Fe-O compounds. The height of the edge crest of the absorption spectrum is proportional to the total amount of Fe in the sample. After normalizing to the edge crest height the peak intensity of Fe in PVG is more than 50% less than that of Fe_2O_3. Therefore this indicates that more than 50% of the Fe in PVG remains as elemental iron or without oxygen as near neighbors. This confirms the previous Mossbauer and EXAFS results which claims more than 50% of the Fe in PVG remain as elemental iron. If there is any tetrahedrally co-ordinated Fe^{3+} ions in the glass samples, which is one possibility for small isomer shift Fe compounds, the pre-edge intensity would be much greater than that of α-Fe_2O_3. Slight increase of pre-edge intensity of Fe in PVG with annealing temperature indicates that part of the elemental iron oxidizes as samples annealed to 650^{0}C and further more as samples heated to 1200^{0}C. This is not surprising because heating were carried out in air. But the majority of Fe remains as elemental iron even after heated to 1200^{0}C.

5.3. Pre-edge feature of glass gels:

Pre-edge features of glass gels impregnated with Fe and heated to 650°C and 1200°C were analyzed using the same methods as those for PVG. Figure 5.3.1 and 5.3.2 a, b, c shows the X-ray absorption spectra, x-ray absorption near edge structure and arctan fit to the main edge, and arctan subtracted normalized pre-edge fit of gels heated to 650°C and 1200°C respectively. Figure 5.3.3 shows the normalized pre-edges of gels together with α-Fe_2O_3 for comparison. Peak positions and intensities are tabulated in Table 5.2. From the figure 5.3.3 it can be seen that in both α-Fe_2O_3 and gels heated to 650°C, the intensity is almost same. In the case of α-Fe_2O_3 all Fe atoms are surrounded by octahedrally co-ordinated six oxygen atoms. Therefore gels heated to 650°C also should have octahedrally coordinated six oxygen atoms. This agrees with the Mossbauer and EXAFS results of gel heated to 650°C. But surprisingly pre-edge of gels heated to 1200°C show enhanced intensity. In this case pre-edge intensity is about twice that of Fe_2O_3. But the peak positions are almost the same. This indicates that the charge state of Fe ions in gels is +3, and in the case of gels heated to 1200°C some ions are tetrahedrally co-ordinated. Because if all the Fe atoms are tetrahedrally co-ordinated pre-edge intensity has to be enhanced by six or seven times that of α-Fe_2O_3. If part of Fe atoms are

tetrahedally coordinated and the rest is octahedrally co-ordinated, the pre-edge intensity is intermediate between 100% octahedral and 100% tetrahedral. In our case pre-edge intensity of gels heated to 1200°C is about 2 times that of α-Fe_2O_3 indicates that approximately 25% of the Fe atoms are tetrahedrally co-ordinated.

Table 5.2: Pre-edge feature results of Fe in glass gels.

Sample	Normalized intensity	Energy eV
α-Fe_2O_3	0.034	7114
Gel heated to 650°C	0.029	7113
Gel heated to 1200°C	0.075	7114

5.4. Summary:

Normalized "pre-edge" feature intensities of all PVG samples are almost the same and approximately one half of the normalized "pre-edge" intensity of α-Fe_2O_3. This indicates that only one half of the Fe atoms are surrounded by oxygen atoms and others remain as elemental iron. Fe-O particles have six oxygen atoms octahedrally co-ordinated. In the samples heated to 650°C or 1200°C a small amount of elemental iron converts to oxide product. But in the case

of glass gels enhanced pre-edge intensity has been observed. Normalized pre-edge intensity is greater than that of α-Fe_2O_3. This indicates that there are Fe atoms which are tetrahedrally co-ordinated. From the comparison of pre-edge intensities one can conclude that in the case of glass gels 25% of the Fe exists in tetrahedrally co-ordinated and the other 75% octahedrally co-ordinated.

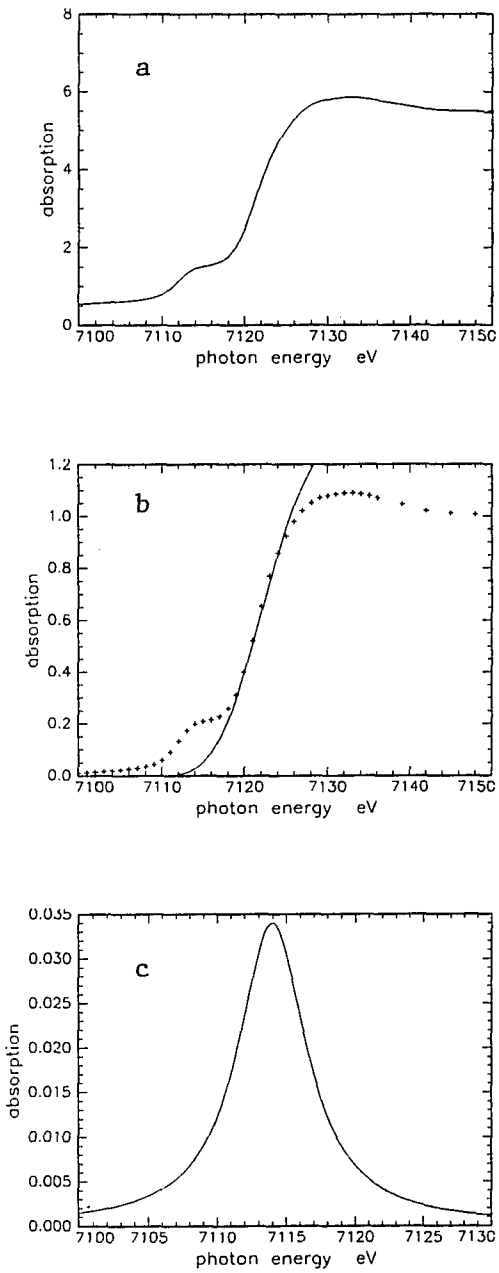

Figure 5.2.1 "Pre-edge" feature data reduction steps of Fe_2O_3.

a) X-ray absorption near edge structure.

b) +++ Data -Arctan fit to the main edge.

c) Arctan subtracted normalized pre-edge.

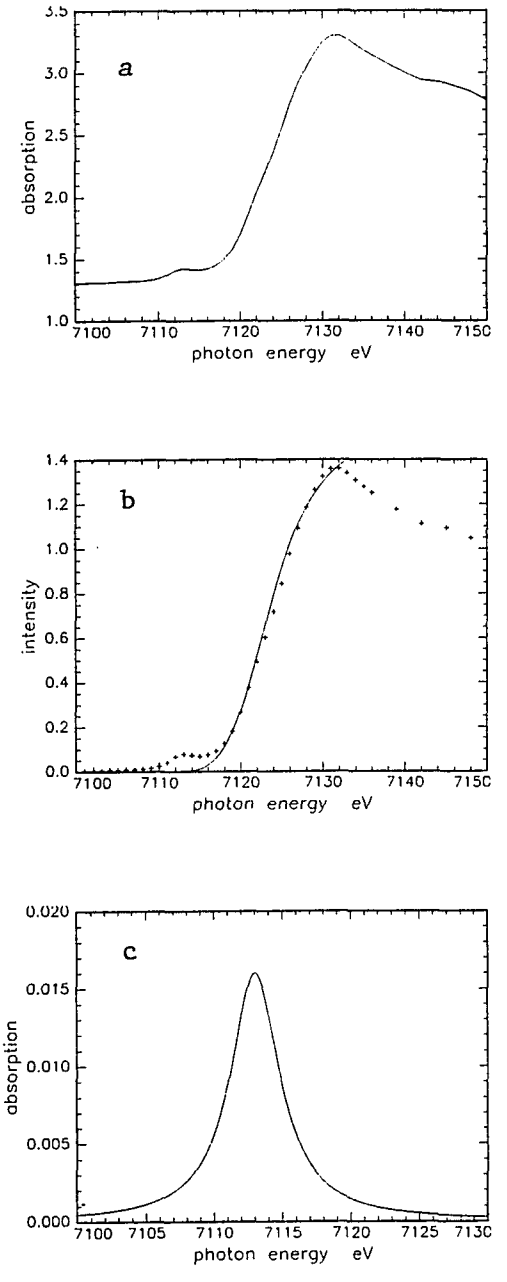

Figure 5.2.2 "Pre-edge" feature data reduction steps of Fe in consolidated PVG.

a) X-ray absorption near edge structure.

b) +++ Data -Arctan fit to the main edge.

c) Arctan subtracted normalized pre-edge.

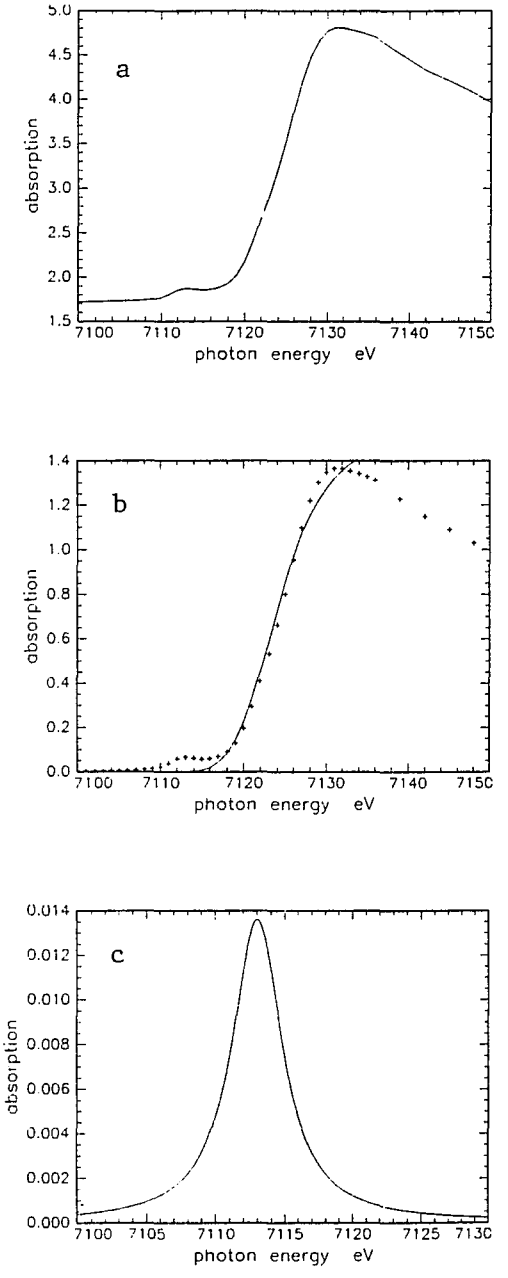

Figure 5.2.3 Data reduction steps of Fe in PVG heated to 650^{0}C.

a) X-ray absorption near edge structure.

b) +++ Data -Arctan fit to the main edge.

c) Arctan subtracted normalized pre-edge.

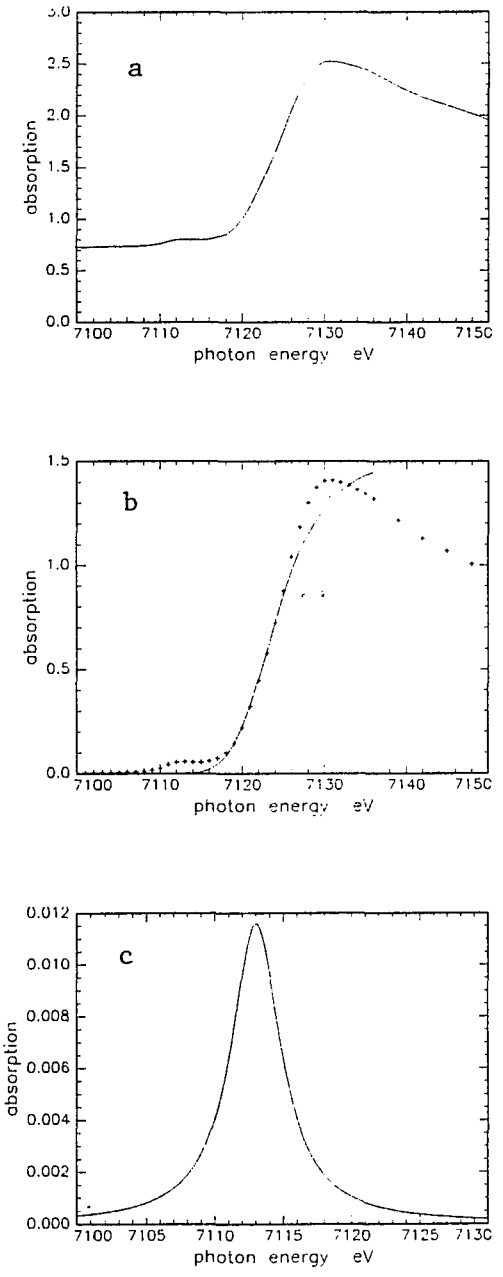

Figure 5.2.4 "Pre-edge" feature data reduction steps of Fe in unheated PVG.

a) X-ray absorption near edge structure.

b) +++ Data -Arctan fit to the main edge.

c) Arctan subtracted normalized pre-edge.

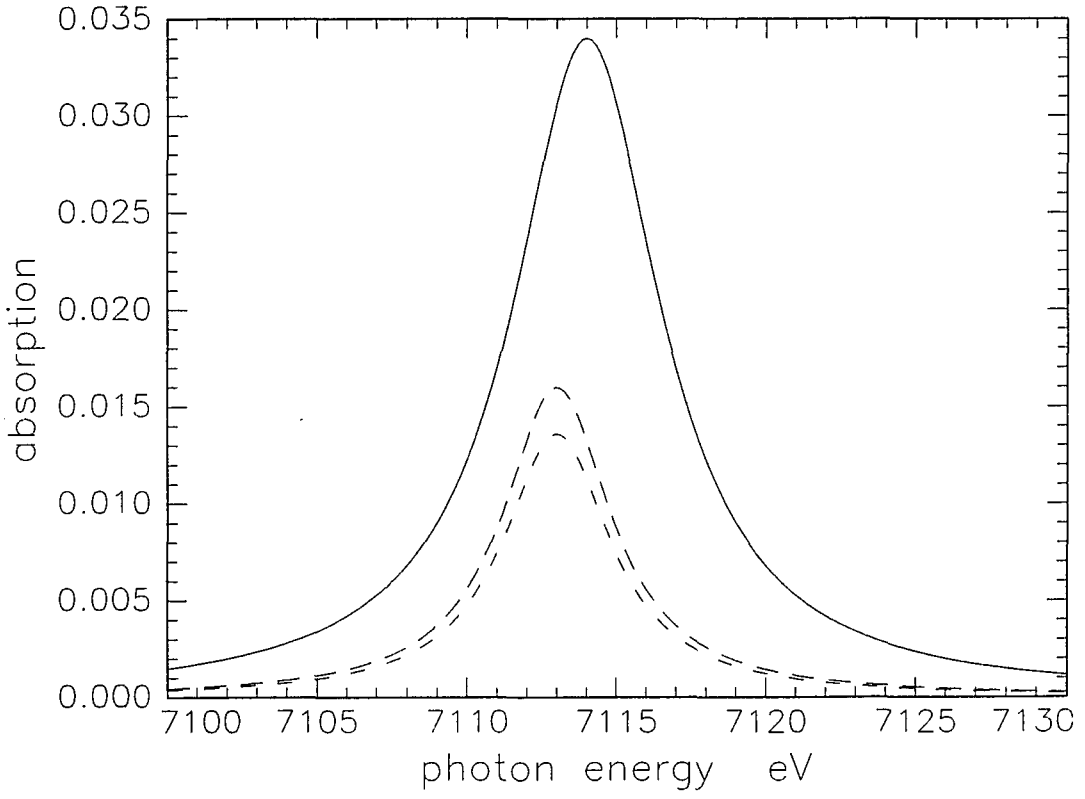

Figure 5.2.5. Normalized pre-edge intensity of α-Fe_2O_3 and Fe in PVG

_ α-Fe_2O_3

-- PVG heated to 1200^{0}C.

_._ PVG heated to 650^{0}C.

...Unheated PVG.

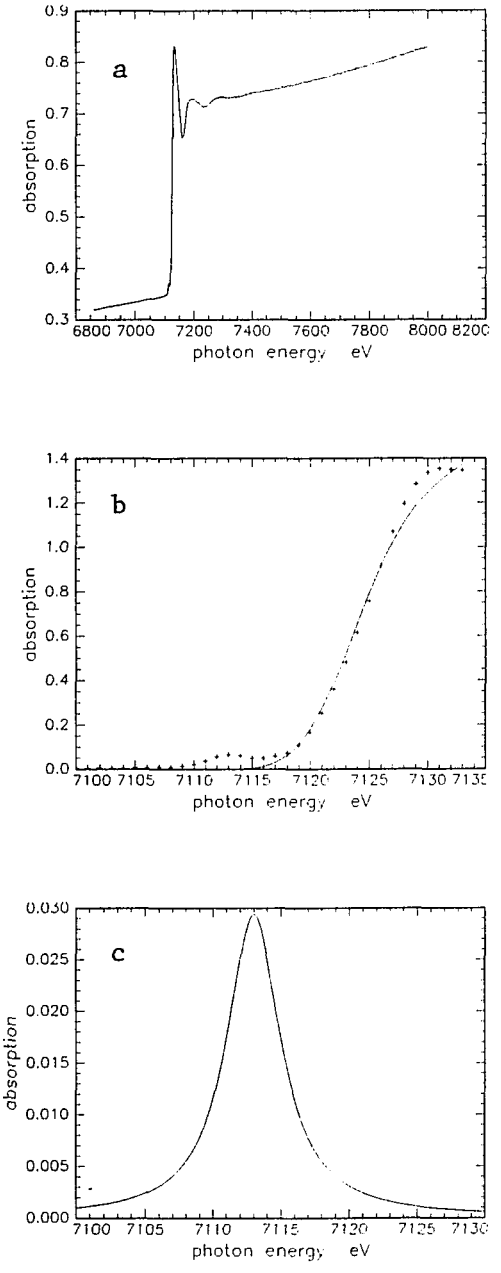

Figure 5.3.1 Pre-edge feature data analysis steps of gel heated to 650^{0}C

a)X-ray absorption spectrum

b) +++ XANES --- Arctan fit to the main edge

c)Normalized pre-edge.

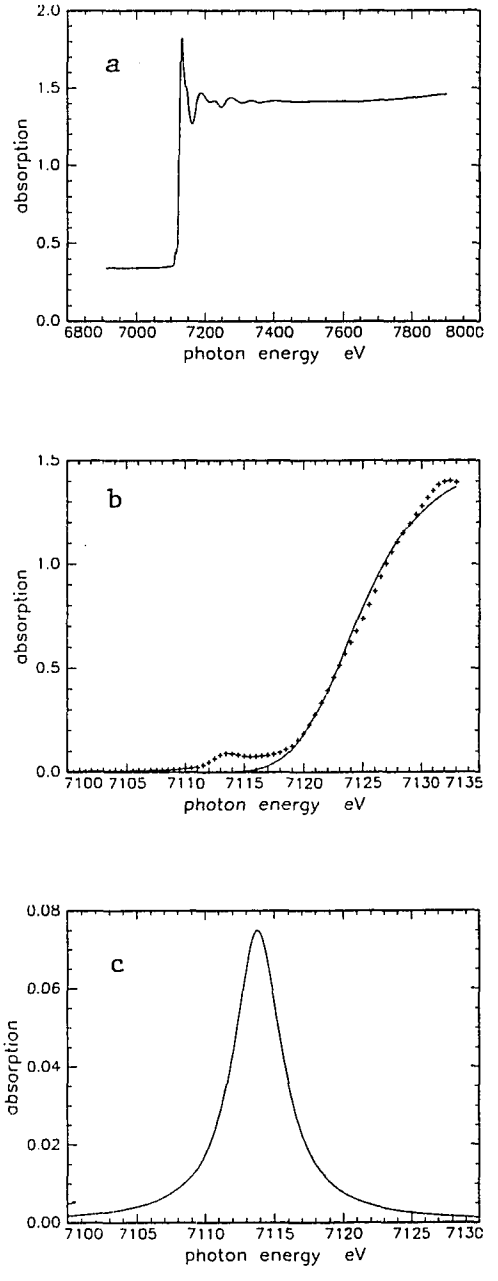

Figure 5.3.2 Data analysis steps of gel heated to 1200^{0}C

a)X-ray absorption spectrum

b) +++ XANES --- Arctan fit to the main edge

c)Normalized pre-edge.

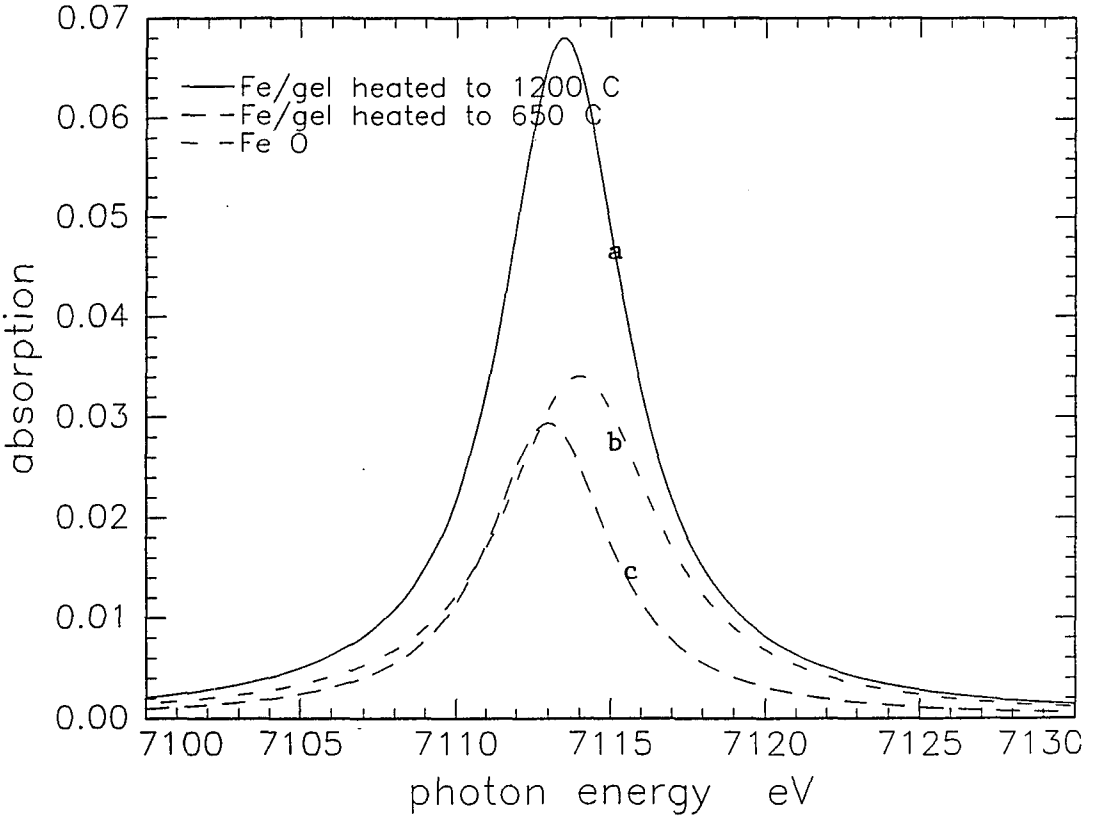

Figure 5.3.3 Normalized pre-edge features of

a) - glass gel heated to 1200^{0}C.

b) -- glass gel heated to 650^{0}C.

c) Fe_2O_3.

CHAPTER 6.

Magnetization and particle size studies.

6.1. Magnetization studies of Fe in PVG.

6.1.1. Introduction:

Control of magnetic anistropy is primarily important for technological applications of magnetic materials such as recording media and magneto-optical devices. One of the best candidates for high coercive force magnetic materials is small Fe particles. Fe particles photodeposited on the glass show different magnetic properties. The Fe on PVG samples heated to 650^{0}C are paramagnetic while in consolidated glass these Fe particles show an ordered structure. The size of these particles can be controlled by annealing temperature.

6.1.2. Results and discussion:

Magnetic properties of the PVG samples impregnated with Fe ind heated to either 650^{0}C or 1200^{0}C were measured using a vibrating sample magnetometer and q SQUID magnetometer at the IBM, Watson Research Center of Yorktown Heights. Figure 6.1.1 shows the magnetization Vs applied field of a PVG sample heated to 1200^{0}C. The saturation magnetization is

approximately 105 e.m.u. per gram of iron in the sample. The magnetization was normalized to the sample weight and then to the weight of Fe in the sample. The weight of Fe in the sample was calculated from the RBS results which gives us the amount of Fe near the surface of the glass relative to silicon and X-ray fluorescence results which shows the distribution of Fe into the interior of the glass. The weight of the Fe in the consolidated glass was 5.72×10^{-3} g per gram of glass and in the glass which is heated to 650°C is about 9.5×10^{-3} g per gram of glass. This saturation magnetization value 105 e.m.u/g is much greater than that of magnetic iron oxides such as Fe_3O_4 or γ-Fe_2O_3. But this value agrees well with the previous assignment of Fe compound to the metallic iron and α-Fe_2O_3. From the Mossbauer, EXAFS, and Pre-edge analysis Fe in the glass was identified as approximately 50% metallic iron 50% α-Fe_2O_3.

The α-Fe_2O_3 is an antiferromagnetic compound and shows very weak ferromagnetism. The saturation magnetization of metallic iron is 218 e.m.u/g. If the half of the iron in the PVG is in the form of metallic iron, the saturation magnetization is 109 e.m.u per gram of iron. This value is very close to the value deduced from PVG, 105 e.m.u/g. The room temperature magnetization curves for samples heated to 1200°C and 650°C are shown in figures 6.1.2 and 6.1.3 respectively. It can be observed that the sample heated to

650^{0}C does not exhibit hysteresis phenomena. The sample heated to 1200^{0}C shows hysteresis at room temperature. These results could be explained by the sizes of particles in the glass matrix. It is a special feature of very small particles that the magnetization vector is not fixed in space, but fluctuates. The effect of such fluctuations depends on their frequency compared to the time scale of the experiment.

6.2 Superparamagnetic relaxation:

Superparamagnetic behavior is typical for small Fe particles[50-57]. In a magnetically ordered solid the direction of the magnetization in a domain is not random, but fixed in some easy directions, cause by the lattice anistropy. The energy barrier which separates the easy directions is given by the product KV of the anistropy constant and particle volume V. The superparamagnetic relaxation is a thermal activated process where the magnetization vector changes its direction across the energy barrier. The relaxation time of a particle of volume V is given by[58]

$\tau=\tau_0\exp(KV/k_BT)$ --------->(6.2.1) where $\tau_0\approx10^{-9}$ sec.

When particles are so small the relaxation can become so fast that within the measuring time of the experiment, in the case of Mossbauer nuclear Larmor precession time, the average magnetization of the particles appears to be zero. This leads to the collapse of the magnetic sextuplet to a

paramagnetic single line or doublet depending on the existence of quadrupole interactions in the particles. Therefore the collapse of a magnetic six line pattern can clearly mark the appearance of superparamagnetism in a fine particle system. This appears to be the case of unheated and heated to 650^{0}C samples which show quadrupole doublets. In the case of 1200^{0}C samples the particles are bigger so relaxation is smaller and average magnetization is not zero and corresponding Mossbauer spectrum shows six lines. In the magnetization measurements we show that the samples heated to 1200^{0}C are ferromagnetic and show hysteresis at room temperature. But the sample heated to 650^{0}C does not show hysteresis which is typical for paramagnetic materials. According to the equation 6.2.1 as the particle gets larger and larger relaxation time gets smaller and smaller. The particle behaves as a ferromagnet and shows hysteresis when the time of observation is smaller than the relaxation time. A particle behaves as a superparamagnet if the time of observation is larger than the relaxation time. One can reduce the thermal vibrations by cooling the sample. Therefore superparamagnetic samples becomes ferromagnetic at a certain temperature. This temperature is known as the blocking temperature. So below the blocking temperature superparamagnets should show Hyperfine fields in Mossbauer spectrum and hysteresis in magnetic measurements. But since observation time for these two kind of experiments is

different, the blocking temperature is also different. But from the Mossbauer and magnetic measurement results we can see that samples heated to 1200°C have both blocking temperatures above the room temperature. The results are not surprising and agrees with the previous studies of similar compounds. Dormann et al[54] have measured the critical diameter of Fe particles in SiO_2 at different temperatures. Their results are summarized in table 7.1.

Temperature	Mossbauer critical diameter	Magnetization critical diameter
4 K	15 Å	10 Å
77 K	45 Å	25 Å
300 K	80 Å	35 Å

Table 6.1. Critical diameters of Fe particles in SiO_2 for Mossbauer and magnetization measurements at different temperatures.

6.3 Hyperfine fields observed in glass:

Two hyperfine fields observed in consolidated glass, 370 kG and 425 kG was assigned as due to elemental iron and α-Fe_2O_3 from the isomer shift and quadrupole splitting values and confirmed from the EXAFS and pre-edge feature analysis. But these values are different from the values of bulk α-Fe and α-Fe_2O_3 which are 330 and 515 kG respectively[28]. The value of 425 kG is closer to the hyperfine fields of Fe_3O_4, B=450 and 500kG[55], than to the hyperfine field of Fe_2O_3. However, the isomer shift data is inconsistent with Fe^{2+} sites, thus the formation of Fe_3O_4 is not likely. In the case of iron oxide particles, the hyperfine fields have been shown to decrease with particle size relative to bulk value[56-58]. According to the model of Morup and Topse[56] the hyperfine field of a particle of volume V is given by $H(V,T)=H(\infty,T)[1-k_B/KV]$ where $H(\infty,T)$ is the bulk value. For 100 Å particles with H=425 kG and bulk value of 515 kG one can calculate K, anistropy constant, as 4.55×10^4 J/m^3. This value agrees with the value calculated from the relaxation time which says K is greater than 2.3×10^3J/m^3. In the case of elemental Fe particles the hyperfine field, 370kG, is somewhat larger than the hyperfine field of bulk α-Fe. But enhancement of the hyperfine field of Fe particles is known to occur on the surface Fe atoms[58]. Due to the large surface to volume ratio, enhancement of the hyperfine field in small Fe aggregates is therefore not surprising. Similar

hyperfine fields 360-390kG have been previously observed in granular Fe-SiO_2 compounds at 4.2 K[59] and 60 Å diameter Fe particles in mercury at 12 K[60]. Hyperfine parameters of these small Fe particles are influenced by neighboring matrix atoms.

6.4. Transmission Electron Microscopy studies:

6.4.1.Introduction:

Electron micrographs of Fe impregnated PVG were taken from Joel 4000 Transmission Electron Microscope(TEM) at Bellcore. The operating voltage was 400,000 volts which is very suitable to study the PVG, because glass samples are relatively thick and for the transmission one needs highly energetic electrons. Fundementally and functionally, electron microscopes and optical microscopes are identical. That is, both types of microscopes serve to magnify minute objects normally invisible to the naked eye. The basic difference between the two, however, is that an electron microscope uses an electron beam as a specimen illuminating medium whereas an optical microscope uses a light beam for this purpose. Ultra high magnification and high resolving power make electron microscope very useful for small particle studies.

6.3.2.Interaction between electron beam and specimen:

When an electron beam passes through a substance, the beam is scattered due to coulomb interactions. The direction of motion of electrons is changed and partial energy loss takes place. As shown in the figure 7.3.1, when electrons having a given energy impringe on a substance, they are changed into transmitted electrons, backscattered electrons and absorbed electrons by the interaction of the aggregate of the atoms in the specimen. The transmitted electrons can be classified into three types.

1.Directly transmitted electrons, which pass through the specimen with little change of direction or wave length.
2.Elastically scattered electrons, which undergo a directional change due to atomic collision but retain their energy.
3.Inelastically scattered electrons which undergo both directional change and partial energy loss.

The ratio of directly transmitted electrons to that of elastically scattered electrons is related to the contrast of images in transmission electron microscopy. The contrast of amorphous specimen images such as glass is primarily

determined by mass thickness. Image contrast is required in order to confirm the presence of an object and to study its configuration. When the specimen is amorphous, the scattered electrons are absorbed by an objective aperture, thus producing scattering absorption contrast. Accordingly, if the scattering is large, most of the electrons will be blocked by the aperture, thus forming the dark portion of the image. The extent to which the electrons are scattered is proportional to the mass thickness of the specimen. Thus, the absorption contrast provides information concerning the existence and configuration(topography) of the object.

6.4.3. Sample preparation:

For the transmission electron microscope samples need to be prepared in very thin form. Otherwise all the electrons absorbed by the sample and no image can be observed. When the accelerating voltage of electrons is 400 kV, sample thickness has to be less than 200 Å. Since we cannot grind the glass to such a thin sample alternate method has to be used. The method we used to prepare the samples are schematically shown in figure 6.4.2. The thickness of the original PVG samples after the photolysis is 2 mm. These 2 mm thick glass samples were mechanically grounded to a thickness of about 200 μm. Then from this grounded glass

was used to cut wedge pieces as shown in the figure 6.4.2(c). The edge of this wedge shape piece is very thin and is now suitable for the TEM observation.

6.4.4. Results and discussion:

The PVG samples prepared under several conditions, such as just after photolyzation, after heat treatment of 650^{0}C, after consolidation for both low and high loadings, were prepared as described in the previous section and examined from high resolution TEM. Figure 6.4.3 is a transmission electron micrograph of PVG just after photolyzation. As can be seen in the figure no particles are visible eventhough this is a high loaded sample. That means Fe exists in this sample as tiny particles probably less than 10 Å in diameter, distributed throughout the glass surface. A micrograph of a sample prepared the same as the earlier one with the same amount of Fe, but after heat treatment of 650^{0}C is shown in the figure 6.4.4. It can be seen that small particles of about 20-30 Å in diameter are visible now. Interparticle distance varies from about 50-100 Å. A micrograph of a consolidated glass with approximately the same iron concentration is shown in the figure 6.4.5. The size of particles of this sample was about 100 Å in diameter and interparticle distance now

varies from 100-500 Å. Fe particles were observed only in high loaded samples. No particles are observed in low loaded samples even after consolidation. This means particles in low loaded samples are very small. From these pictures it is obvious that there is a direct correlation between heat treatment and size of the particles. From the figures 6.4.4 and 6.4.5 we can see that as the size of the particles increases particle density decrease or interparticle distance increases. This we can regard as due to aggregation of nearby particles with the increase of temperature. These Fe clusters just after photolyzation may contain only a few Fe atoms and are so small one cannot see them in high resolution TEM micrograph(Figure 6.4.3). As the samples are heated to 650°C the clusters grow up to about 30 Å in diameter (Figure 6.4.4). The results can be explained by taking into account the mobility of the ions in the glass during the thermal treatment. When the temperature of the sample is 600-650°C the iron particles can move towards each other and form microcrystals whose size is increasing with increasing temperature. As the temperature of the sample increases to 1200°C the pores of the glass collapsed and samples become non porous uniform glass. This helps several small clusters to aggregate further to form a large cluster. The average size of these clusters, as seen from Fig 6.4.5, is about 100 Å in diameter. Change of the size of Fe particles in silicate

glass with temperature has been previously reported[61]. As the local Fe concentration is increased, the size of the precipitate particles increases.

6.4.5. Summary:

The size of the Fe particles photodeposited in glass increases with increasing temperature. In the unheated sample the Fe particles are not visible and probably smaller than 10 Å in diameter. But in the samples heated to 650°C and 1200°C the particles are clearly visible and the average diameters are 30 Å and 100 Å respectively. The sample with particles 100 Å diameter shows ferromagnetic properties and the other samples with smaller particles show superparamagnetic properties. These changes were explained by the relaxation time of small particles. The saturation magnetization value agrees with the previous Mossbauer, EXAFS, and Pre-edge results which indicate about half of the Fe in the sample is elemental Fe and the rest is α-Fe_2O_3.

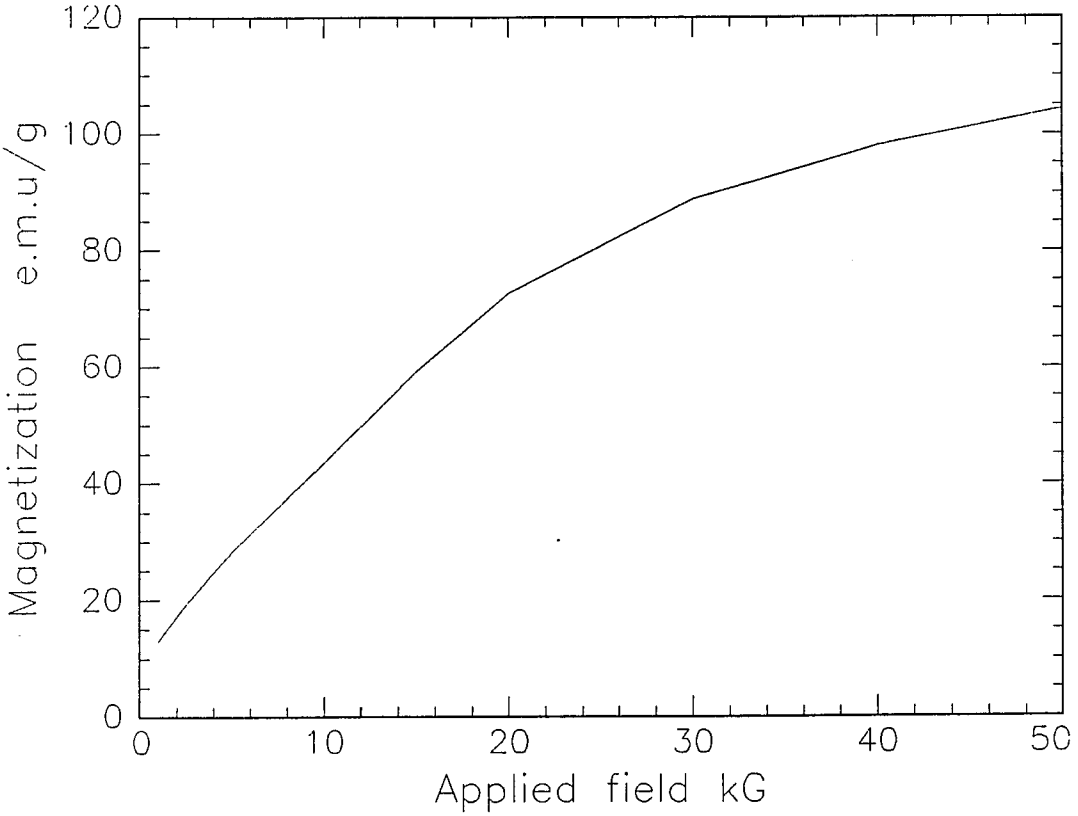

Figure.6.1.1. Magnetization curve of PVG heated to 1200^{0}C at 5 K.

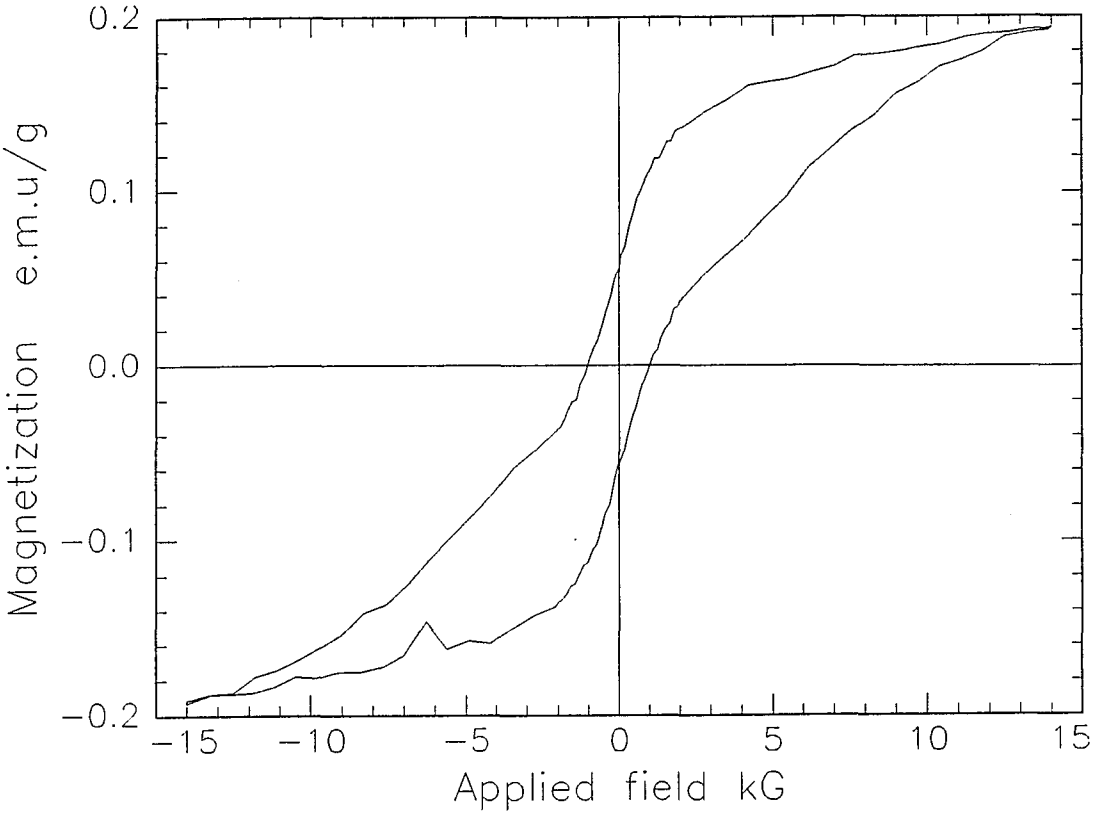

Figure 6.1.2 Room temperature hysterisis of Fe in PVG heated to 1200°C.

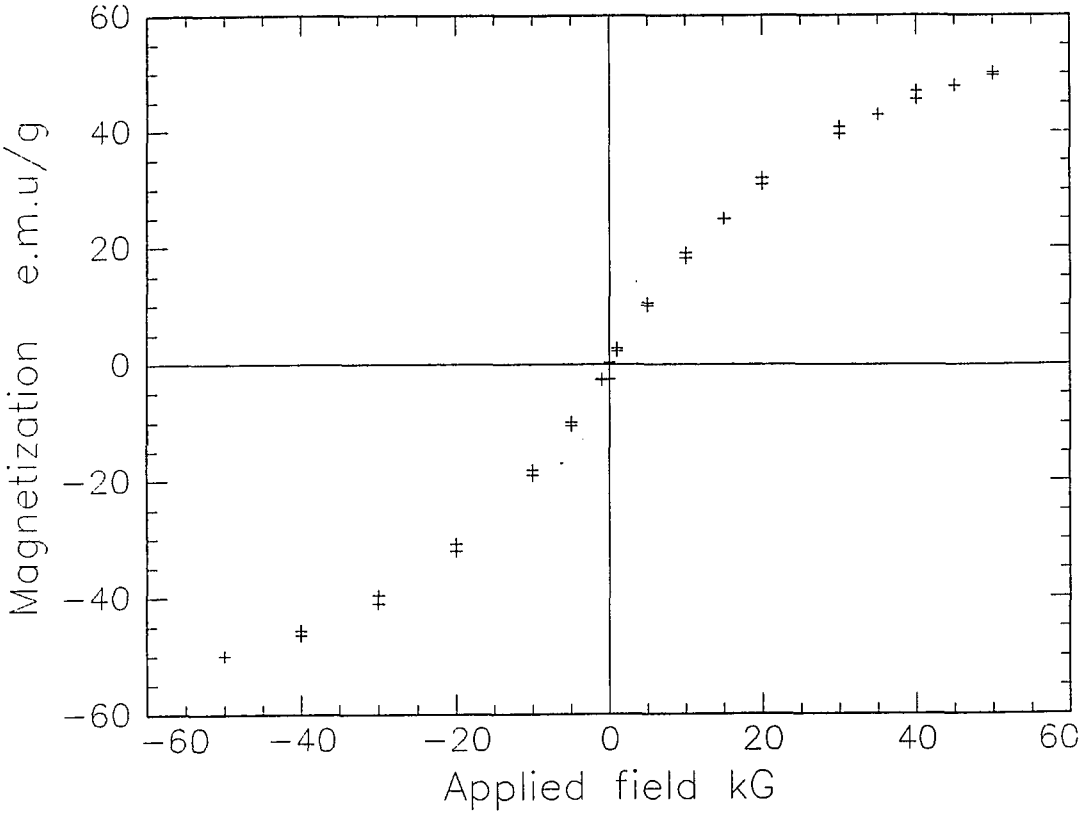

Figure 6.1.3. Room temperature magnetization curve for Fe in PVG heated to 650^{0}C.

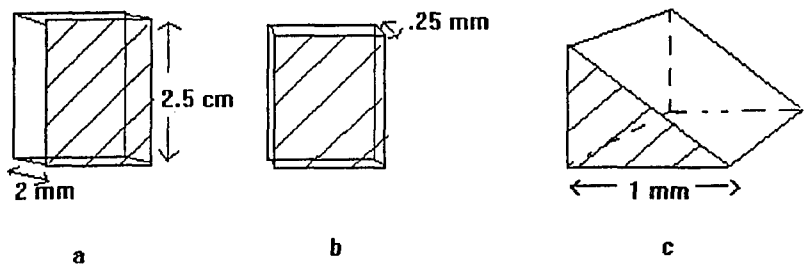

Figure 6.4.1. TEM sample preparation steps. Shaded side of the glass was photolyzed.

a)original PVG after photolyzation.

b)after mechanically grinding to a thickness of about 200 μm.

c)wedge shape piece cut from the glass of part b.

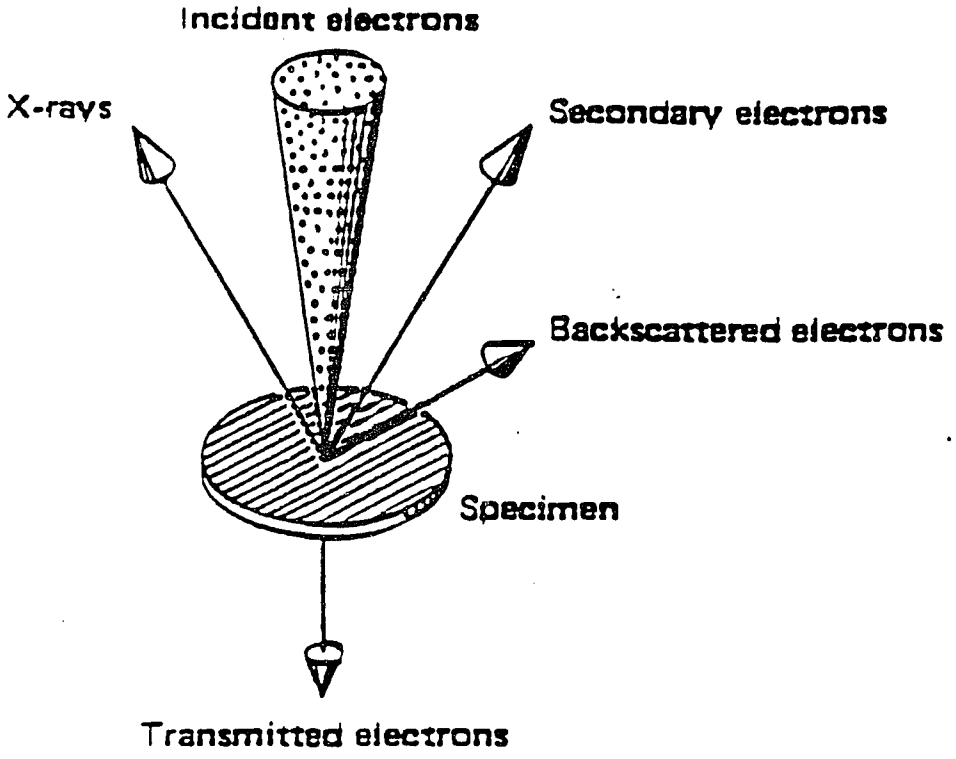

Figure 6.4.2. Interaction between specimen and electron beam.

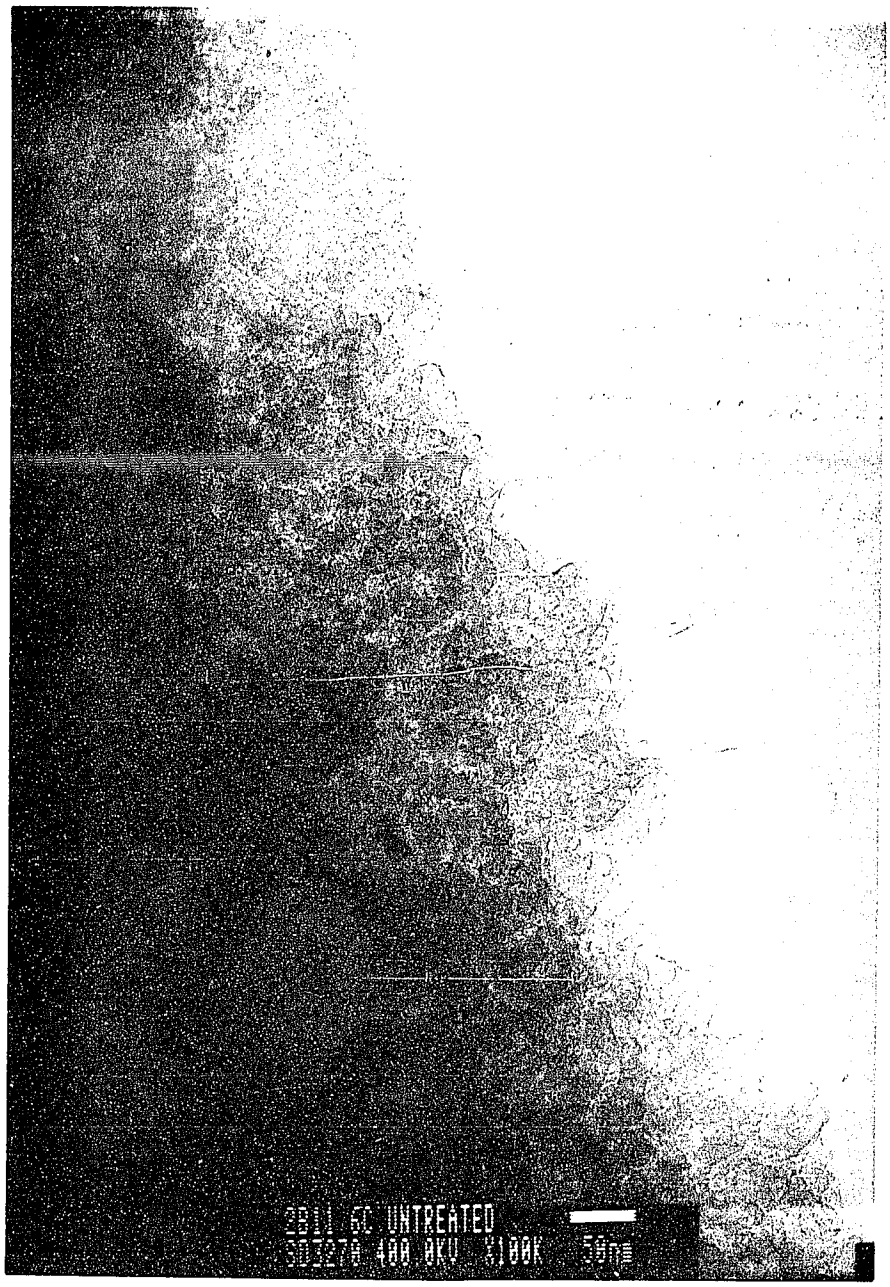

Figure 6.4.3. TEM micrograph of PVG just after photolyzation.

Figure 6.4.4. TEM micrograph of PVG heated to 650°C.

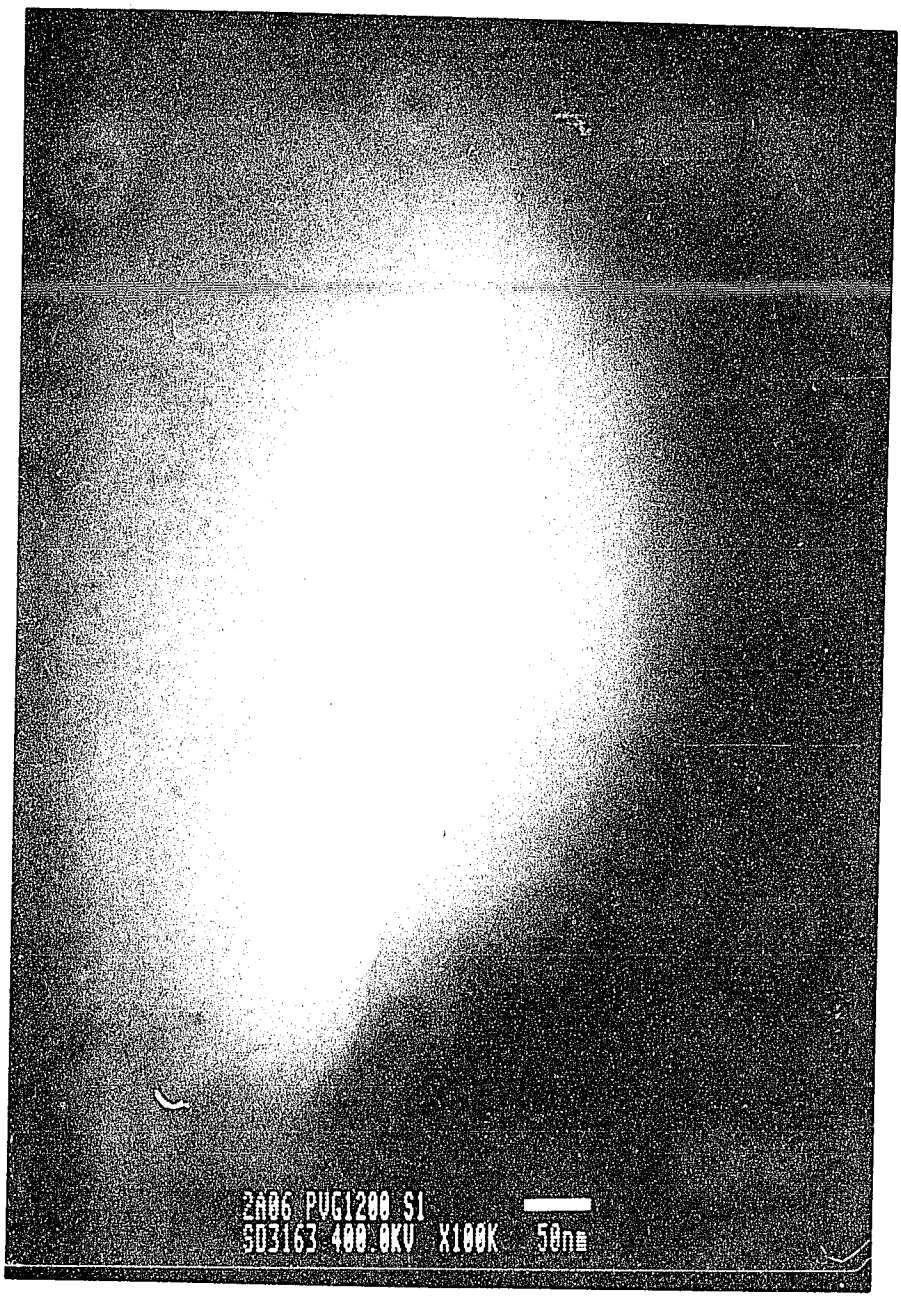

Figure 6.4.5. TEM micrograph of consolidated PVG.

Conclusion:

From the X-ray fluorescence and Mossbauer results we can conclude that the photolysis process binds the iron compound to the surface of the glass. All the experimental results, Mossbauer, EXAFS, Pre-edge, and Magnetization measurements agree with two different type of Fe products. One similar to elemental iron with other iron atoms at 2 Å as nearest neighbors and the other a Fe-O compound with each iron atom surrounded by six oxygen atoms at about 1.8 Å. Heating of the glass to 650°C or 1200°C does not affect the composition of the Fe products. But as the heating temperature increases iron particles aggregate to form larger particles. These can be seen in TEM pictures and their presence also explains the Mossbauer hyperfine patterns observe in the glass samples heated to 1200°C. Mossbauer spectra of PVG samples heated to 650°C show paramagnetic doublets at liquid nitrogen temperature which indicates that the blocking temperature of these samples are below 77K.

Apendix

EXAFS studies of Er doped Tellurite glasses.

Introduction:

Erbium doped glasses were first investigated for eye safe laser rangefinders, but more recently have received a great deal of attention as fiber amplifiers for the 1.55 μm telecommunications window[61-64]. Fiber gains in excess of 5 dB/mW of absorbed power with total gains greater than 35dB have been achieved in silicate glasses. However, it is always interesting to study the behavior of rare earths in glass hosts other than silicates and hopefully new features can be developed. Tellurite glasses have been chosen because they have very high indeces of refraction(~1.65-2.32), large nonlinear refractive indeces (25 times higher than silica), and a relatively low phonon energy spectrum(peak values ~800 cm^{-1}). Although selected properties of some rare earths in tellurite glasses have been described in the literature[65-67], the work has not previously been extended to the fabrication of active devices such as fiber laser oscillators and amplifiers. Erbium doped tellurite glasses have shown unique optical properties and therefore well suited for these devices. To improve these devices the role of erbium in the glass has to

be fully understood. From the EXAFS we can study the local environment of erbium in tellurite glasses.

Results and discussion:

X-ray absorption data of erbium doped tellurite glasses were obtained by fluorescence method near L_3 edge and analyzed using usual methods as described earlier. Figures 1a-1d and 2a-2d show the data analysis steps of erbium in glass and Er_2O_3 respectively. Phase shift values and backscattering amplitude function were obtained from the Er_2O_3 standard. Figure 1d was obtained using the same phase shift and amplitude function as erbium oxide. The Er-O distance is 2.23 Å, which is slightly less than the Er-O distance in erbium oxide. Number of near neighbors, N, we cannot determine accurately because of high correlation between disorder term σ and N. But if we assumed the disorder of glass is same as that of erbium oxide, then best fit can be obtained with 8.4 oxygen atoms. Since the disorder of glass is usually higher than crystalline materials the actual number of near neighbors could be less than 8 and possibly equal to 6 which is the number for erbium oxide. Since the data we fitted only using single shell of oxygen atoms, erbium is not directly bound to the glass. It is either loosely bound to the glass via oxygen atoms or stay neutral randomly in the glass matrix.

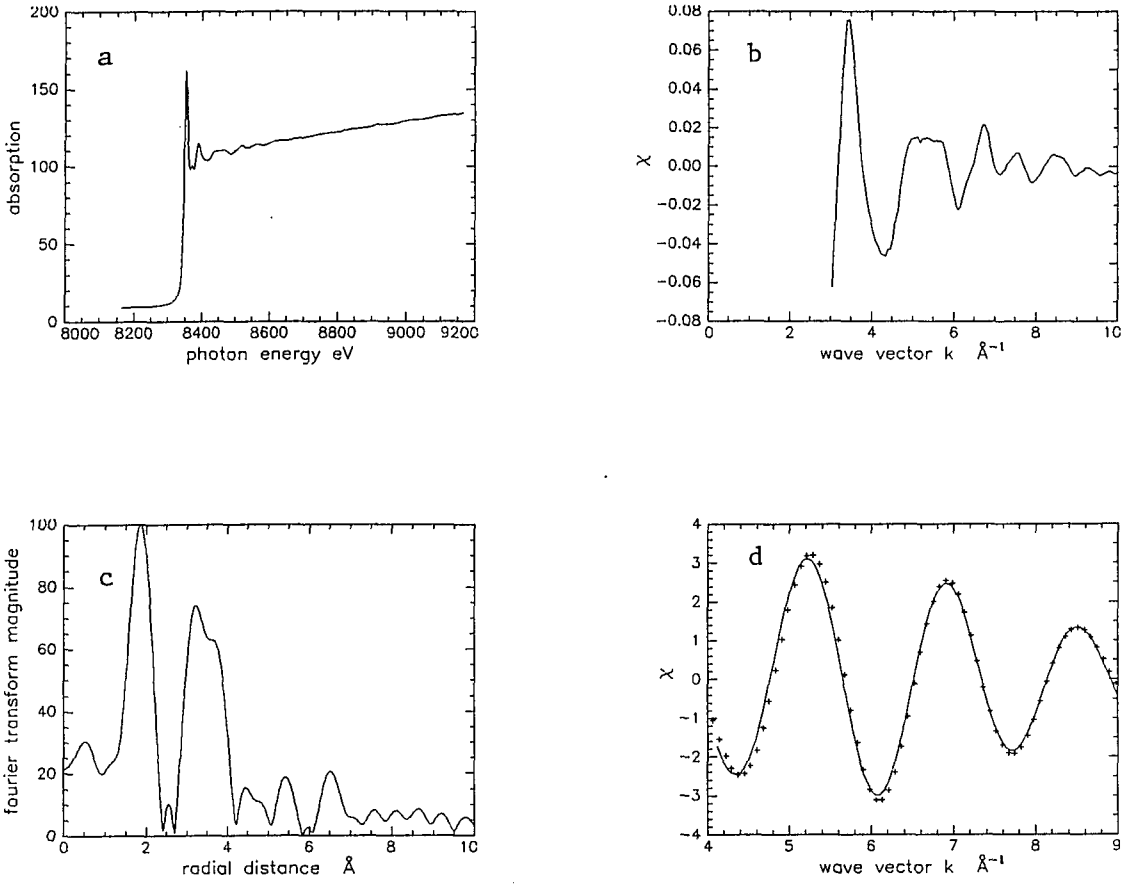

Figure 1. EXAFS data reduction steps of Er_2O_3.

a) X-ray absorption spectrum.

b) Background subtracted χ function.

c) Radial distribution function.

d) Backtransformed first peak of RDF and one oxygen shell fit.

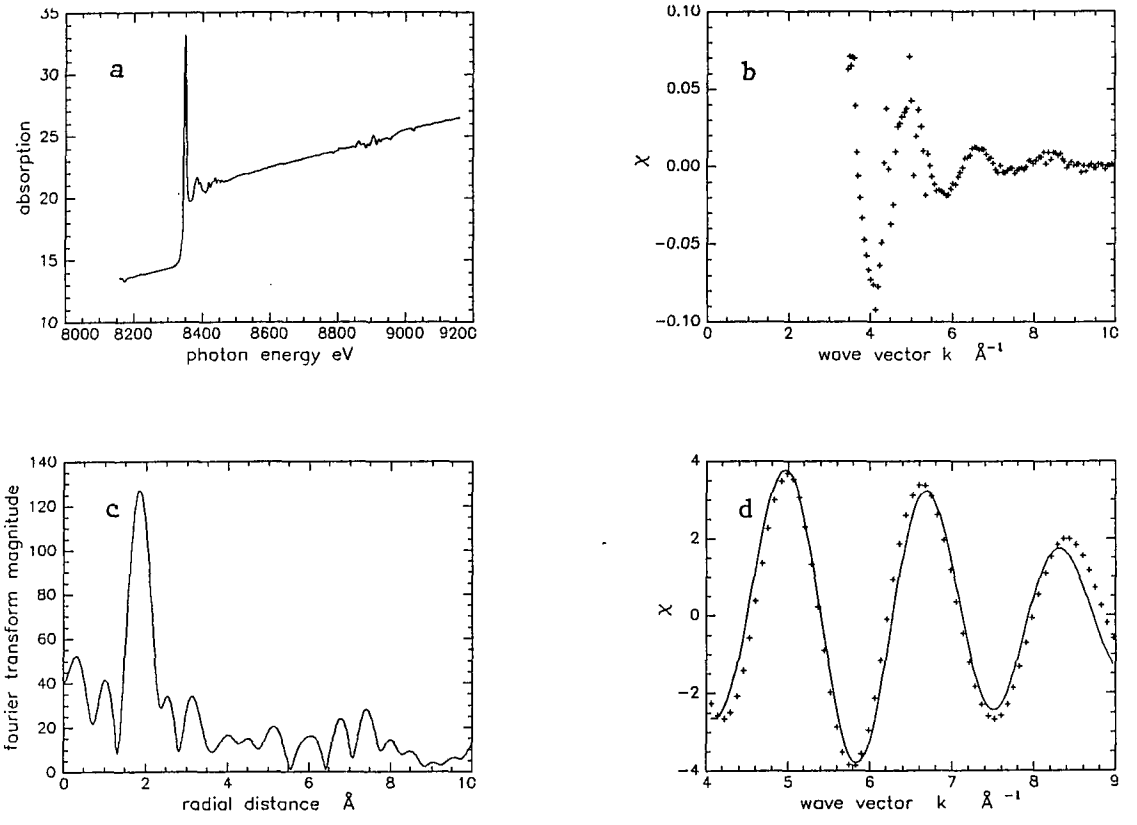

Figure 2. EXAFS data reduction steps of Er in glass.

a) X-ray absorption spectrum.

b) Background subtracted χ function.

c) Radial distribution function.

d) Backtransformed first peak of RDF and one oxygen shell it.

Bibliography:

1)N.F.Borrelli and D.L.Morse, Appl.Phy.Lett 43,992(1983).

2)N.F.Borrelli, D.L.Morse, J.H.Scheurs J.Appl.Phys. 54,6(1983).

3)N.F.Borrelli, M.D.Cotter, J.C.Luong, IEEE J.Quantum Electronics QE-22,896(1986).

4)H.D .Gafney, J.Imag.Sci 33,27(1989).

5)E.A.Mendoza, E.Wolkow, D.Sunil, P.Wang, J.Sokolov, M.H.Rafailovich, M.denBoer,H.D.Gafney, Langmuir 7,3046(1991).

6)O.Horie, Y.Syono, Y.Nakagama, A.Ito, K.Okamura, S.Yajima, Solid.State.Commu. 25,423(1978).

7)E.Hanga, L.Diamandescu, M.Morariu, N.Popescu-Pogrion, E.Tataru, Proc.Intl.Conf.Mossbauer spectroscopy 1977 Romania page 423.

8)B.O.Myson, J.Non.Cryst.Solids 95&96,247(1987).

9)W.Muller-Warmuth, H.Eckert, Physics Reports 88,91(1982).

10)R.R.Bukrey, P.F.Kenealy, G.B.Beard, H.O.Hooper, Phy.Rev.B 9,1052(1974).

11)S.S.Sekhon, R.Kamal, J.Appl.Phy 49,3444(1978).

12)C.R.Kurkjian, J.Non.Cryst.Solids 3,157(1970).

13)Methods of surface analysis. Ed. J.M.Walls. Cambridge university press. Cambridge. 1990 page 300.

14)Mossbauer spectroscopy. P.E.Dickson and F.J.Berry. Cambridge University press. Cambridge. 1986 page 5.

15)R.L.Mossbauer Z.Physik, 151,124,(1958).

16) L.R.Walker, G.K.Wertheim, V.Jaccarino, Phy.Rev.Lett. 6,98(1961).

17) E.Simanek, Z.Sroubek, Phy.Rev. 163,275(1967).

18) Mossbauer spectroscopy. Ed. U.Gonser. Springer-Verlag. New York 1975. Page 26.

19) Mossbauer spectroscopy. Ed. U.Gonser. Springer-Verlag. New York 1975. Page 20.

20) H.Polllak, M.De Coster, S.Amelinokx, Mossbauer effect in Amorphous substances Eds. D.M.J.Compton and D.Sehue Mossbauer effect P298, Wiley New York.

21) M.Darby Dyar, American Minerologist 70,304-316,1985.

22) J.W.Park, H.Chen, Physics and chemistry of glasses 23,107-108(1982).

23) H.H.Wickman and G.K.Wertheim in Chemical applications of Mossbauer spectroscopy. Ed. V.I.Goldanski and R.H.Herber. Academic press New York(1968).

24) R.R.Bukrey, P.F.Kenealy, G.B.Beard, H.O.Hooper Phy.Rev B 9,1052(1974).

25) W.Kundig, H.Bommel, G.Constabaris, R.H.Lindquist, Phy.Rev.142,327(1966).

26) T.Yoshioka and H.Ikoma, Jpn. J.Phy 38,77(69).

27) R.A.Levy J.Phy Colloq, 47,613,(1983).

28) Z.Zhongshen, Y.Yisong, H.Zhimin, L.R.Ougehnan, X.Yuanfu, W.Shuxin, J.Non.Cryst.Solids 84,34(1986).

29) O.C.Kistner and S.Sunyar, Phy.Rev.Lett. 4,412(1960).

30) EXAFS spectroscopy:Techniques and applications Teo B.K., Joy D.C.(Eds) PlenumPres, New York P 13-58.

31) B.K.Teo and P.A.Lee, J.Am.Chem.Soc. 101,2815(1988).

32) S.G.Saxena, K.B.Garg, Phys.Status.Solidi 87,K25(1985).

33) P.A.Montano, G.K.Shenoy, Solid State Commu. 35,53,(1980).

34) A.Bianconi, EXAFS for inorganic systems(Edited by C.D.Garner and S.S Hasman) 13,(1981).

35) G.A.Waychunas, M.J.Apted, and G.E.Brown, Phy.Chem.of Minerals 10,1(1983).

36) N.Motta, M.De Crescenzi, and A.Balzarotti, Phy.Rev.B 27,4712(1983).

37) E.H.White, H.A.McKinstry, Adv.X-ray Anal 9,376-392(66).

38) U.C.Srivastava, H.L.Nigam, Co-od Chem Rev 9,275-310(1973).

39) G.Calas, W.A.Bassett, J.Petiau, M.Steinberg, D.Tchoubar, A.Zarka, Phy.Chem.Minerals 11,17-36(1984).

40) A.Bianconi, A.Giovannelli, Solid State Commu. 42,547(1982).

41) C.N.Greaves, J.Non-Cryst.Solids 71,203,(1985).

42) C.H.Chou, J.Guo, D.E.Ellis Phy.Rev B 34,12(1986).

43) G.Calas, J.Petiau Solid.State.Commu 48,625(1983).

44) R.G.Shulman, Y.Yafet, P.Eisenberger, W.E.Blumberg, Proc.Natl.Acad.Sci. U.S.A. 73,1384(1976).

45) G.A.Waychunas, Proc.Geol.Soc.Am.Annu.Meet. 12,545(1980).

46) J.A.Tossell, D.J.Vaughan, K.H.Johnson, Am.Mineral. 59,319(1974).

47) S.I.Salem, C.N.Chang, P.L.Lee, P.Severson, J.Phy. C 11,4085(1978).

48) P.R.Sarode, S.Ramasesha, W.H.Madhusudan, C.N.R.Rao, J.Phy. C 12,2439(1976).

49) A.Kumar, A.N.Nigam, U.Agarwala, Jpn.J.Appl.Phys.18,2299(1979).

50) P.Auric, J.Chappert, A.K.Badyopadyoy, J.Zarzyclki, J.Phy.Collq. 40,278(1979).

51) S.Morup, H.Topsoe, App.Phy 11,73(76).

52) S.Morup, H.Topse, J.Lipka, J.Phy.Colloq 37,C6-287(1976).

53) K.Hadeda, A.H.Morrish, Phy.Lett 64,259(1977).

54) J.L.Dormann, PGibart, G.Suran, C.Sella, Physica 86-88B,1431(1977).

55) J.L.Dormann, P.Gibart, R.Renaudin, J.Phy.Collq 37,C6-281(1976).

56) R.Bauminger, S.G.Cohen, A.Marinov, S.Ofer, E.Segal, Phy.Rev.122,1447(1961).

57) J.L.Dormann, J.R.Cui, C.Sella, J.Appl.Phys. 57,4283(1985).

58) S.Morup, H.Topsoe, J.Lipka, J.Phy.Colloq. 37,C6-287(1976).

59) T.Shinjo, M.Kiyama, N.Sujita, K.Watanabe, T.Takada, J.Magn & Magn Mate. 35,133(1983).

60) J.L.Dormann, C.Sella, P.Renaudin, A.Kaba, P.Gibart, Thin solid films 58,265(1979).

60) S.Linderoth and S.Morup, J.Appl.Phy 67,4496(1990).

61) E.Snitzer, H.Po, F.Hakimi, R.Tumminelli and B.C.McCallum, Optical fiber communications conference, 1988, New Orleans, Louisiana. Post deadline paper PD2.

62) R.J.Mears, L.Reekie, I.M.Jaunceey, N.Payne, Electron.Lett. 23,1026(1987).

63) E.Desurvire, J.R.Simpson, P.C.Becker, Opt.lett.12,888(1987).

64) M.J.Creaner, D.Spirit, G.R.Walker, R.C.Steele, J.Mellis, S.A.Chalabi, W.Hale, I.Sturgees, M.Rutherford, D.Trivett, and M.Brian, Electron Lett. 26,442(1990).

65) R.Reisfeld and Y.Eckstein, J.Non.Cryst.Solids, 15, 125(1974).

66) A.A.Bahgat, E.E.Shaisha, A.I.Sabry, J.Mat.Sci. 22,1323(1987).

67) M.J.Weber, J.D.Myers and D.H.Blackburn, J.Appl.Phy, 52,2944(1981).